Monthly Notices
of the
ROYAL ASTRONOMICAL SOCIETY

MNRAS **492,** 2347–2368 (2020)
Advance Access publication 2019 December 24

doi:10.1093/mnras/stz3590

MUSE-ALMA haloes V: physical properties and environment of $z \leq 1.4$ H I quasar absorbers

Aleksandra Hamanowicz [1]★, Céline Péroux,[1,2] Martin A. Zwaan,[1] Hadi Rahmani,[3] Max Pettini,[4] Donald G. York,[5] Anne Klitsch [1,6], Ramona Augustin [7], Jens-Kristian Krogager [8], Varsha Kulkarni,[9] Alejandra Fresco,[10] Andrew D. Biggs [1], Bruno Milliard[2] and Joël D. R. Vernet [1]

[1]*European Southern Observatory, Karl-Schwarzschild-Str 2, D-85748 Garching near Munich, Germany*
[2]*Aix Marseille Université, CNRS, LAM (Laboratoire d'Astrophysique de Marseille) UMR 7326, F-13388 Marseille, France*
[3]*GEPI, Observatoire de Paris, PSL Research University, CNRS, Place Jules Janssen, F-92190 Meudon, France*
[4]*Institute of Astronomy, University of Cambridge, Madingley Road, Cambridge CB3 0HA, UK*
[5]*Department of Astronomy and Astrophysics, The Enrico Fermi Institute, University of Chicago, 5640 S. Ellis Ave, Chicago, IL 60637, USA*
[6]*Department of Physics, Centre for Extragalactic Astronomy, Durham University, South Road, Durham DH1 3LE, UK*
[7]*Space Telescope Science Institute, 3700 San Martin Drive, Baltimore, MD 21218, USA*
[8]*Institut d'Astrophysique de Paris, CNRS-SU, UMR7095, 98bis bd Arago, F-75014 Paris, France*
[9]*Department of Physics and Astronomy, University of South Carolina, Columbia, SC 29208, USA*
[10]*Max-Planck-Institut für extraterrestrische Physik (MPE), Giessenbachstrasse 1, D-85748 Garching bei Müchen, Germany*

Accepted 2019 December 18. Received 2019 December 18; in original form 2019 September 9

ABSTRACT

We present results of the MUSE-ALMA haloes, an ongoing study of the circumgalactic medium (CGM) of low-redshift galaxies ($z \leq 1.4$), currently comprising 14 strong H I absorbers in 5 quasar fields. We detect 43 galaxies associated with absorbers down to star formation rate (SFR) limits of 0.01–0.1 $M_{\odot}$ yr^{-1}, found within impact parameters (b) of 250 kpc from the quasar sightline. Excluding the targeted absorbers, we report a high detection rate of 89 per cent and find that most absorption systems are associated with pairs or groups of galaxies (3–11 members). We note that galaxies with the smallest impact parameters are not necessarily the closest to the absorbing gas in velocity space. Using a multiwavelength data set (UVES/HIRES, *HST*, MUSE), we combine metal and H I column densities, allowing for derivation of the lower limits of neutral gas metallicity as well as emission-line diagnostics (SFR, metallicities) of the ionized gas in the galaxies. We find that groups of associated galaxies follow the canonical relations of N(H I)–b and $W_r(2796)$–b, defining a region in parameter space below which no absorbers are detected. The metallicity of the ISM of associated galaxies, when measured, is higher than the metallicity limits of the absorber. In summary, our findings suggest that the physical properties of the CGM of complex group environments would benefit from associating the kinematics of individual absorbing components with each galaxy member.

Key words: galaxies: abundances – galaxies: haloes – intergalactic medium – galaxies: absorption lines.

1 INTRODUCTION

Galaxies grow, evolve, and sustain their star formation, thanks to the accretion of gaseous material from filaments of the cosmic web (Martin et al. 2012; Rubin et al. 2012). In turn, strong outflows from supernovae or AGN feedback expel enriched material out of the galaxies (Shull, Danforth & Tilton 2014), some of which comes back in the form of galactic fountains (Fraternali 2017), while some is carried away from the system by galactic winds. Most of the gas recycling and inflow happens within a few hundreds of kiloparsec from the galaxy centre in a region dubbed the circumgalactic medium (CGM). These extended gaseous haloes surrounding galaxies are transition zones where inflowing intergalactic medium (IGM) material meets metal-enriched gas expelled from galaxies (Tumlinson, Peeples & Werk 2017).

Investigating the physical processes taking place within the CGM is key to understanding galactic evolution. However, studies of these extended regions in emission are challenging due to the low surface brightness of the gas (Frank et al. 2012; Corlies et al. 2018; Augustin

★ E-mail: ahamanow@eso.org

et al. 2019). So far, emission from the CGM has only been detected around extreme ionization sources, like luminous quasars, in the form of gigantic filamentary Ly α nebulae (Cantalupo et al. 2014; Borisova et al. 2016; Arrigoni Battaia et al. 2019; Lusso et al. 2019; Umehata et al. 2019). and using deep MUSE exposures, around faint galaxies at redshift $z = 3$–6 (Wisotzki et al. 2018). To study the CGM around typical star-forming galaxies, we must rely on distant bright point-like light sources such as quasars or gamma-ray bursts whose light gets attenuated by the material around a foreground galaxy (Bouché et al. 2007; Péroux et al. 2011; Christensen et al. 2017). Various absorption lines, from the most abundant Ly α, to numerous metal lines like Mg II, Fe II, or C IV, originating in the intervening systems can reveal information about kinematics and metallicities of the absorbing medium. Metals can, in principle, be used as tracers of gas flows in the CGM. Lehner et al. (2013), Quiret et al. (2016), and more recently Wotta et al. (2019), observed a bimodality in the metallicity distribution of the low-redshift quasar absorbers, possibly a trace of metal-poor inflows and metal-rich outflows.

Understanding the physical properties of the CGM is at present best constrained observationally by the identification of the host galaxies linked to the gas observed in absorption. Historically, the first associated galaxy candidates have been identified on wide-field images of the quasar field as the closest object to the quasar sightline (Bergeron et al. 1988; Bergeron & Boissé 1991; Steidel, Dickinson & Persson 1994; Le Brun et al. 1997). By using long-slit spectroscopy, it was then possible to confirm the redshifts of these objects (Fynbo et al. 2010, 2013; Rahmani et al. 2016). Supplementary to the wide-field search was the method of using a narrow-band (NB) optical filter (about 10 Å) centred around the expected [O II] emission at the absorbers' redshift (Yanny et al. 1987; Yanny, York & Gallagher 1989; Yanny, York & Williams 1990a; Møller & Warren 1993). Another detection method involved surveying the quasar field with an X-Shooter slit triangulation in search for associated galaxies (Møller, Fynbo & Fall 2004; Krogager et al. 2017). Narrow filter integral field searches, using an array of optic fibres, for extended emission near QSOs with absorbers were also attempted (Yanny et al. 1990b).

Integral-field spectroscopy with instruments like SINFONI (Eisenhauer et al. 2003), MUSE (Bacon et al. 2006), or OSIRIS (Larkin et al. 2006) make it possible to obtain spectra of many sources in the field of view and efficiently classify galaxies associated with absorbers. Combined with high-resolution UV spectroscopy of quasars, these studies have revealed relevant features interpreted as galactic outflows (Schroetter et al. 2016; Rahmani et al. 2018b; Schroetter et al. 2019), warped accretion discs (Rahmani et al. 2018a), and galactic fountains (Bouché et al. 2016).

Alongside the detection of kinematic traces of gas inflows and outflows, new studies detected multiple galaxies associated with one absorber (Bielby et al. 2017; Péroux et al. 2017; Klitsch et al. 2018; Nielsen et al. 2018; Muzahid et al. 2019; Péroux et al. 2019). These findings point towards a more complex view of the gaseous haloes of galaxies: from the halo gas of single systems, through tidal streams and halo substructures (Whiting, Webster & Francis 2006; Kacprzak, Murphy & Churchill 2010) to intra-group gas (Bielby et al. 2017; Fossati et al. 2019). All these studies have, however, focused on single-absorber systems or on single-species absorbers such as O VI (e.g. Bielby et al. 2019) or Mg II (Zabl et al. 2019), lacking the information about the H I, which is crucial for metallicity estimates. At higher redshifts, some damped Ly α absorbers (DLAs; with $\log[N(\mathrm{H\,I})/\mathrm{cm}^{-2}] \geq 20.3$) and Lyman Limit Systems (LLSs; $\log[N(\mathrm{H\,I})/\mathrm{cm}^{-2}] \leq 19.0$) have been found to be associated with multiple Ly α emitters (LAEs; Lofthouse et al. 2019; Mackenzie et al. 2019). In this work, we undertake a statistical analysis of H I-selected absorbers. We present a MUSE study of 5 quasar fields with 14 H I absorbers at $z \leq 1.4$, to perform a statistical study of the properties of the absorbers and their associated galaxies, including their metallicities. Each of these fields also has associated ALMA observations, targeted to detect CO(2–1) and CO(3–2) emission lines from galaxies associated with H I-rich quasar absorbers. Measuring the molecular content of these systems makes it possible to constrain the physical properties and kinematics of molecular gas, known to be the fuel of star formation (forthcoming publication).

Table 1. Parameters of the quasars in MUSE-ALMA halo sample: (1) reference name used in this paper, (2) full name of the quasar, (3) right ascension, (4) declination, and (5) quasar redshift.

QSO name	Alternative name	RA [hh:mm:ss]	DEC [dd:mm:ss]	z
Q0152−2001	UM 675	01:52:27	−20:01:07.1	2.06
Q1130−1449	B1127−145	11:30:07	−14:49:27.7	1.19
Q1211+1030	1209+107	12:11:41	+10:30:02.8	2.19
Q1232−0224	1229−021	12:32:00	−02:24:04.6	1.05
Q2131−1207	Q2128−123	21:31:35	−12:07:04.8	0.43

This paper is organized as follows. In Section 2, we describe the data and the reduction process, and in Section 3 we present the analysis details and the results. In Section 4, we discuss our findings, comparing them to previous studies, and we summarize the study in Section 5. Images and spectra of all absorbers and associated galaxies can be found in the appendix.

We adopt the following cosmology: $H_0 = 70$ km s^{-1} Mpc^{-1}, $\Omega_\mathrm{M} = 0.3$, and $\Omega_\Lambda = 0.7$.

2 MUSE OBSERVATIONS AND ANCILLARY DATA

The MUSE-ALMA halo sample of quasar absorbers is based on five quasars observed with MUSE and archival high-resolution UV spectroscopy: Q0152−2001, Q1130−1449, Q1211+1030, Q1229−0207, and Q2131−1207; quasars coordinates and redshifts are summarized in Table 1. Throughout the paper, we refer to these quasars with their first four right ascension numbers (e.g. Q1130). Similarly, we adopt the naming scheme for the absorbers in our sample: first four right ascension numbers + z + the redshift of the absorber [up to second decimal point (e.g.Q1229z076)].

The MUSE quasar fields were selected (proposal 096.A-0303(A), PI: Péroux) for the presence of known H I absorbers, with column density $\log[N(\mathrm{H\,I})/\mathrm{cm}^{-2}] > 18.5$ at redshift $z \sim 0.4$, for which MUSE covers all prominent galactic emission lines: H β, [O II], [O III], H α, [N II], and [S II]. Furthermore, for all selected quasars, at least one galaxy was known to be associated with this H I absorber, identified with photometry or low-resolution spectroscopy [Q0152 – Rao et al. (2011), Q1130 − Kacprzak et al. (2011), Q1211 − Kacprzak et al. (2011), Q1232 − Le Brun et al. (1997), and Q2131 − Kacprzak et al. (2011)].

2.1 High-resolution UV/optical quasar spectroscopy

We used UVES/VLT and HIRES/Keck archival high-resolution spectra for all five quasars in our sample to identify absorbers and their multiple metal absorption lines. Q0152−2001 and Q2131−1207 were observed with HIRES/Keck at resolution $R =$ 45 000–48 000. The remaining quasar spectra (Q1130−1449,

Q1211+1030, and Q1232−0224) were covered by the VLT/UVES spectrograph BLUE arm, with combined exposure times from 4 to 6 h and spectral resolution up to $R = 80\,000$. The wavelength coverage differs between objects due to different initial observation set-ups, introducing gaps in the spectra. The data were uniformly reprocessed using the ESO UVES pipeline and individual exposures of each target were merged, weighted by their signal-to-noise ratios (Zafar, Popping & Péroux 2013).

We also used archival *HST*/FOS spectra covering the H I absorption line for all the absorbers in our sample. We used the already reduced FOS UV spectra from the *HST* archives for Q1232−0224 (PI: Bergeron, ID:5351, FOS-G190H, $R = 1300$, $T_{\rm exp} = 4580$ s) and Q1130−1449 (PI: Deharveng, ID: 3483, FOS-G160L, $R = 250$, $T_{\rm exp} = 1450$ s). For the remaining systems, we relied on the measurements of H I column density from the literature (references included in Table 2).

We note that the wavelength reference frame differs for MUSE (air) and UVES/HIRES (vacuum). To obtain precise redshift and velocity measurements, we shifted the MUSE spectra to a vacuum wavelength reference system.

2.2 MUSE and *HST* imaging of five quasar fields

The five quasar fields we present in this work were observed with VLT/MUSE IFU in period 96 [proposal 096.A-0303(A), PI: Péroux]. All observations were conducted in good seeing conditions (<0.85 arcsec) with an average of 1–2 h per target for all but field Q1130−1449 (Péroux et al. 2019), which was significantly deeper (12 × 1200 s). All fields were observed in 'nominal mode', resulting in a spectral coverage of 4800–9300 Å.

All raw MUSE observations of our quasar fields were reduced with the ESO default MUSE reduction pipeline v2.2 (Weilbacher, Streicher & Palsa 2016). We applied bias, flat and wavelength calibration, and line spread functions as well as illumination correction frames to each individual exposure with the *scibasic* command, creating MUSE-specific PIXTABLE output. The astrometry solution and the correction for geometry, together with flux calibrations, were all combined within the *scipost* command. Finally, individual exposures were combined including field rotation. The detailed description of the reduction procedure can be found in Péroux et al. (2019). We refrained from using the pipeline sky subtraction method, due to unsatisfactory results. Instead, removal of sky emission lines was performed on the final data cube with a Principal Component Analysis (PCA) algorithm (Husemann et al. 2016). The code creates PCA component of selected sky regions used further to remove sky residuals.

In addition to MUSE observations, we used readily available, reduced archival *HST* imaging for the galaxy identification: WFPC2 (Wide Field Planetary Camera 2) in filter *F702W* of quasars Q0152−2001 (PI: Steidel, ID:6557), Q1211+1030, Q1232−0224 (PI: Bergeron, ID:5351), and Q2131−1207 (PI: Maccheto, ID:5143) and WFC3 (Wide Field Camera) IR-F140W of Q1130−1449 (PI: Bielby, ID: 14594), with exposure times from 10 to 50 min. An example of MUSE and corresponding *HST* WFPC2 quasar field images for Q1232z083 is shown in Fig. 1.

3 ANALYSIS AND RESULTS

3.1 Identification of H I and metal absorbers in high-resolution UV quasar spectra

High-resolution UV quasar spectra are used for the identification of the metal absorbers and measurements of the metal-line column densities. Together with far-UV measurements of H I column density, this allowed us to measure metallicities of the observed gas. The primary sample is comprised of known strong H I absorbers; we used the high-resolution UV spectra to identify the metal lines associated with these absorbers. Specifically, we identified Fe II (Fe II λλ 2382, 2344, 2586, and 2600), which we use for the metallicity measurements. We then expanded the sample to other metal absorbers by identification of the characteristic lines such as Mg II or C IV doublets down to the equivalent width limit of $W_{\rm r}(2796) > 0.02$. For the redshift determination, we used Mg II λ2796; in case of multiple components, we used the strongest one to measure the central wavelength. We limited the sample to systems with redshift $z < 1.4$, so that the [O II] emission line is within the MUSE wavelength coverage, resulting in a list of 14 Mg II absorbers, of which some have been presented elsewhere: Q0152z038 (Rahmani et al. 2018a), Q0152z078 (Rahmani et al. 2018b), Q1130z031 (Péroux et al. 2019), and Q2131z042 (Péroux et al. 2017). We used VPFIT[1] v10.0 to fit the Voigt profiles to unsaturated metal absorption lines. In particular, we fitted Fe II of systems whose metallicities were not known from the literature. We referred to the measurements of H I column densities [N(H I)] in the literature, and for missing cases (Q1211z089, Q1211z105, Q1232z076, and Q1232z083) we measured it used the archival *HST* FOS UV spectra. We derived [Fe/H] metallicities of the absorbing gas using a solar metallicity value of $[{\rm Fe/H}]_\odot = -4.5$ from Asplund et al. (2009). However, Fe is not a perfect tracer of the metallicity since it is well known that this element can be depleted on to dust.

Dust in the gas associated with the absorber could cause reddening of the quasar spectrum. To test if there is a significant amount of dust associated with the absorbing gas, we fit the spectral templates to quasars optical spectra extracted from MUSE cubes and archival optical and near-infrared photometry. The details of the method can be found in Appendix A. We estimate the reddening to be $E(B-V) = 0.02$–0.03 for all quasars in the sample, indicating that the that Fe depletion on to dust in absorbers is likely small. Given the remaining uncertainty in the dust correction, we considerably refer to absorption metallicity estimates as lower limits.

3.2 Ionization correction for low N(H I) absorbers from Bayesian MCMC approach

Apart from the dust, the absorption metallicity measurement can be affected by the H ionization fraction. Most absorbers in our sample are not DLAs [$\log(N({\rm H\,I})) < 20.3\,{\rm cm}^{-2}$] and in such systems we expect a significant portion of the hydrogen to be ionized, influencing the metallicity derivations. To assess the effect of the ionization correction on the metallicities derived for such absorbers, we used the radiative transfer calculations from CLOUDY (Ferland et al. 2013). We performed Bayesian MCMC modelling on the pre-computed grid of Cloudy models from Fumagalli, O'Meara & Prochaska (2016). The grid consisting of multiple radiative transfer models is defined by four parameters: N(H I) [$\log(N({\rm H\,I})) = 17.0$–$20.5$], redshift ($z = 0.0$–$4.5$), metallicity [$\log(Z/Z_\odot) = (-4.0)$–$(1.0)$], and $n_{\rm H}$ density [$\log(n_{\rm H}) = (-4.5)$–(0.0)]. N(H I) and redshift are constrained from the observations and serve as an input. To determine the most probable model, we use as constraints the measured metal-line column densities (Mg II, Mg I, and Fe II in almost all cases). We run the MCMC chain over the grid, using

[1] https://www.ast.cam.ac.uk/~rfc/vpfit.html~rfc/vpfit.html

Table 2. Parameters of the absorbers and their associated galaxies. Each absorber row is followed by the rows of associated galaxies. Absorber parameters: (1) AbsorberID: first part of the quasar name + the absorber redshift, selection method in brackets, (2) ID of the quasar, (3) redshift of the quasar, (4) redshift of the absorber, (5) column density of H I, (6) equivalent width of Mg II λ2796, (7) absorber [Fe/H] (not dust corrected), and (8) corresponding figures in the appendix (position on the sky and spectra of associated galaxies). Each galaxy parameter row consists of: (1) Galaxy ID, in the order of increasing impact parameter, unless the nomenclature adapted from literature states differently (Q1130z031, Q1130z032), (2) redshift of the galaxy, (3) impact parameter in kpc and arcsec, (4) observed magnitude of the galaxy in the *HST F702W* filter if the galaxy was detected (unless marked otherwise), (5) star formation rate (SFR) measured from [O II] emission line flux (not dust corrected) (Kobulnicky, Kennicutt & Pizagno 1999), and (6 and 7) 12 + log(O/H) (not dust corrected): we report both metallicity branches following Kobulnicky et al. (1999); in case of literature values where only one metallicity was reported, we leave the upper metallicity column blank. Literature references: [a]Kacprzak et al. (2011), [b]Lane et al. (1998), [c]Muzahid et al. (2016), [d]Rao, Turnshek & Nestor (2006), [e]Boisse et al. (1998), [f]Rahmani et al. (2018b), [g]Péroux et al. (2019). [1]Observed magnitudes in *HST F814W* from Kacprzak et al. (2010).

Absorber ID Galaxy	Quasar ID z_{gal}	z_{QSO} b [kpc arcsec^{-1}]	z_{abs} HST_{mag} *F702W*	log[N(H I)/cm^{-2}] SFR$_{[OII]}$ [M$_\odot$ yr^{-1}]	W_r(2796) [Å] 12+log(O/H)$_{lower}$	[Fe/H] 12+log(O/H)$_{upper}$	Figure
Q0152z038 (H I)	**Q0152−2001**	**2.06**	**0.3887**	**<18.8**[f]	**0.58 ± 0.05**[a]	**> −1.36**	**B1, -**
G1	0.3826	60/11.5	–	1.04 ± 0.03	8.65 ± 0.09	–	
G2	0.3802	80/15.4	–	0.33 ± 0.01	8.70 ± 0.07	–	
G3	0.3815	86/16.5	–	0.31 ± 0.01	8.42 ± 0.06	–	
G4	0.3814	123/23.7	–	0.12 ± 0.02	8.94 ± 0.08	–	
G5	0.3814	172/33.1	–	<0.02	–	–	
G6	0.3824	205/39.4	–	0.07 ± 0.01	7.82 ± 0.13	–	
Q0152z078 (Mg II)	**Q0152−2001**	**2.06**	**0.7800**	**$18.87^{+0.11}_{-0.14}$**[d]	**0.36 ± 0.04**[d]	**> −0.44**	**B1, -**
G1	0.7803	54/7.6	–	23.00 ± 5	7.90 ± 0.20	8.60 ± 0.20	
Q1130z019 (Mg II)	**Q1130−1449**	**1.19**	**0.1906**	**<19.1**	**0.14 ± 0.01**	**–**	**B2, B7**
G1	0.1905	17/5.3	22.26	–	–	–	
Q1130z031 (H I)	**Q1130−1449**	**1.19**	**0.3127**	**21.71 ± 0.07**[b]	**2.21 ± 0.12**[d]	**−1.94 ± 0.08**[g]	**B3, -**
G0	0.3131	11/2.3	–	0.07 ± 0.1	8.64 ± 0.14	–	
G1	0.3121	18/3.8	21.55[1]	2.80 ± 0.8	8.12 ± 0.08	–	
G2	0.3127	44/9.5	18.81[1]	0.44 ± 0.3	8.77 ± 0.05	–	
G4	0.3126	82/17.7	18.64[1]	>0.40	<8.65	–	
G6	0.3115	98/21.3	19.79[1]	1.14 ± 0.7	8.94 ± 0.16	–	
G16	0.3133	21/4.5	–	0.42 ± 0.1	7.96 ± 0.14	–	
G17	0.3136	35/7.6	22.50	3.18 ± 0.7	8.01 ± 0.17	–	
G18	0.3125	27/5.9	–	0.30 ± 0.1	8.69 ± 0.18	–	
G19	0.3119	120/26.0	21.43[1]	1.09 ± 0.2	8.67 ± 0.16	–	
G20	0.3140	56/12.1	21.82[1]	<0.01	–	–	
G21	0.3122	131/28.4	24.67[1]	0.01 ± 0.01	8.76 ± 0.17	–	
Q1130z032 (Mg II)	**Q1130−1449**	**1.19**	**0.3283**	**<18.9**	**0.028 ± 0.003**[a]	**–**	**B3, B8**
G3	0.3282	74/15.3	20.12[1]	0.02 ± 0.01	7.52 ± 0.28	8.93 ± 0.09	
G5	0.3284	87/18.2	18.84[1]	0.006 ± 0.001	–	–	
Q1211z039 (H I)	**Q1211+1030**	**2.19**	**0.3929**	**19.46 ± 0.08**[d]	**1.19 ± 0.01**[a]	**>1.05**	**B4, B9**
G1	0.3928	37/6.8	21.93	4.71 ± 0.08	8.16 ± 0.01	8.48 ± 0.01	
Q1211z062 (H I)	**Q1211+1030**	**2.19**	**0.6296**	**$20.30^{+0.18}_{-0.30}$**[d]	**2.92 ± 0.23**[d]	**−0.98 ± 0.3**[e]	**B4, B10 (Fig. 2)**
G1	0.6283	12/1.7	21.59	1.04 ± 0.14	–	–	
G2	0.6303	132/19.1	24.53	0.59 ± 0.05	–	–	
Q1211z089 (Mg II)	**Q1211+1030**	**2.19**	**0.8999**	**<18.50**	**0.023 ± 0.005**	**–**	**B4, B11**
G1	0.8991	79/10.0	24.65	4.33 ± 0.43	–	–	
G2	0.8995	185/23.4	23.26	2.03 ± 0.19	–	–	
G3	0.8991	275/34.8	–	0.57 ± 0.07	–	–	
G4	0.8953	149/18.9	24.37	3.29 ± 0.14	–	–	
G5	0.8960	197/24.9	–	1.68 ± 0.21	–	–	
Q1211z105 (Mg II)	**Q1211+1030**	**2.19**	**1.0496**	**<18.90**	**0.18 ± 0.01**	**> −1.69**	**–**
No galaxies found to match the absorber							
Q1232z039 (H I)	**Q1232−0224**	**1.05**	**0.3950**	**20.75 ± 0.07**[e]	**2.894 ± 0.11**	**<−1.31**[e]	**B5, (Fig. 2)**
G1	0.3953	8/1.5	23.00	0.67 ± 0.09	8.02 ± 0.06	8.66 ± 0.04	
Q1232z075 (Mg II)	**Q1232−0224**	**1.05**	**0.7572**	**$18.36^{+0.09}_{-0.08}$**[d]	**0.52 ± 0.07**[d]	**> −1.48**	**B5, B13**
G1	0.7566	68/9.1	22.89	2.58 ± 0.23	8.54 ± 0.19	8.19 ± 0.19	
Q1232z076 (Mg II)	**Q1232−0224**	**1.05**	**0.7691**	**18.11 ± 0.15**	**0.053 ± 0.001**	**> −2.34**	**B5, B14**
G1	0.7666	57/7.7	22.11	3.85 ± 0.14	–	–	
G2	0.7685	131/17.5	–	0.84 ± 0.07	8.06 ± 0.14	8.55 ± 0.10	
G3	0.7688	170/22.7	21.62	<1.41	–	–	

Table 2 – *continued*

Absorber ID Galaxy	Quasar ID z_{gal}	z_{QSO} b [kpc arcsec^{-1}]	z_{abs} *HST*$_{mag}$ *F702W*	log[N(H I)/cm^{-2}] SFR$_{[OII]}$ [M$_\odot$ yr^{-1}]	W_r(2796) [Å] 12+log(O/H)$_{lower}$	[Fe/H] 12+log(O/H)$_{upper}$	Figure
Q1232z083 (Mg II)	**Q1232−0224**	**1.05**	**0.8311**	**18.84 ± 0.10**	**0.238 ± 0.004**	**>−2.19**	**B5, B15**
G1	0.8309	122/15.8	22.73	3.10 ± 0.25	–	–	
G2	0.8323	166/21.6	–	<0.70	–	–	
G3	0.8325	176/22.8	21.84	5.42 ± 0.29	–	–	
G4	0.8321	182/23.6	–	0.61 ± 0.13	–	–	
Q2131z043 (H I)	**Q2131−1207**	**0.43**	**0.4298**	**19.50 ± 0.15**[c]	**0.41 ± 0.01**[d]	**>−0.96**	**B6, -**
G1	0.4301	52/9.2	20.54	2.00 ± 0.2	8.98 ± 0.02	–	
G2	0.4307	61/10.7	–	0.20 ± 0.1	8.32 ± 0.16	–	
G3	0.4301	147/26.0	–	0.08 ± 0.1	–	–	
G4	0.4298	174/30.7	–	0.10 ± 0.1	–	–	

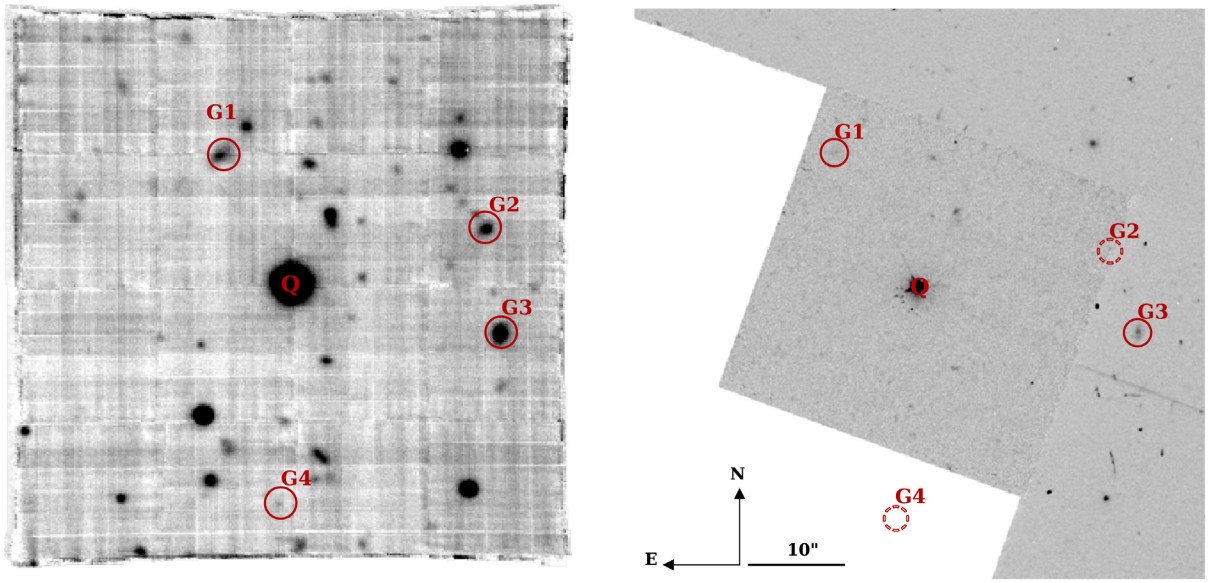

Figure 1. MUSE white light (left) and *HST* F702W (right) images of the Q1232z083 absorber field. Galaxies associated with this absorber are marked with red circles. Non-detections are marked with dashed circles: both galaxies G4 and G2 are undetected in the *HST* image, G4 because it falls outside the field of view of the WFPC2 camera, and G2 because it is at the edge between two camera chips. The MUSE and the *HST* images in the figure are both centred around the background Q1232−0224 (zQSO = 1.05). This figure illustrates the power of IFU observations to identify galaxies associated with absorbers. Images of the remaining fields from the sample with galaxies associated with the absorbers marked on them are presented in the appendix.

the PYIGM package routines.[2] For the resulting probability density functions of each of the parameters, we adopt the median value of the computed [Fe/H] metallicity (see Table 2). For a detailed description of the method, its extension, and assumptions in the UV background, we refer the reader to Fumagalli et al. (2016) and Wotta et al. (2019).

3.3 Identification of galaxies associated with absorbers

After the identification of all quasar absorbers, we used the MUSE observations of the quasar fields, together with wide-field imaging with *HST* WFPC2 to search for galaxies associated with these absorbers. We used several analysis techniques to maximize the completeness of the search, including different types of objects (SF-galaxies, passive galaxies, faint, low-SFR objects, etc.). MUSE data cubes can be viewed as individual NB images at each wavelength slice or a combined continuum image over the whole observed wavelength range, allowing for two types of object searches in the data: a single spectral-line search at the redshift of the absorber and identification of the sources seen in continuum. We combined 50 (50 × 1.25 Å) MUSE wavelength planes into a pseudo-NB image centred at the expected [O II] observed wavelength at the redshift of the absorbers. The choice of the width of the pseudo-NB corresponds to a velocity difference to the absorber redshift of Δv ± 1000–1500 km s^{-1}, depending on the central wavelength of the observed [O II] line. The slight redshift dependence is a mild effect that is mitigated by the systemic search with MUSELET. Then, we identified all bright sources on the NB images and inspected their full spectra to confirm the redshift by the presence of other emission lines (if detected). This allows us to detect galaxies at a range of impact parameters, from systems close to the quasar (<1 arcsec) up to the limits imposed by the MUSE field of view. Within the spectral coverage of MUSE, [O II] doublet can be observed up to $z = 1.4$; however, from $z = 0.8$ it will be the only prominent galactic line covered. We exclude the possibility of the contamination from the low-z sources ($z < 0.8$), because at that redshift range we would

[2]PyIGM Package is available at https://github.com/pyigm/pyigm (Prochaska et al. 2017).

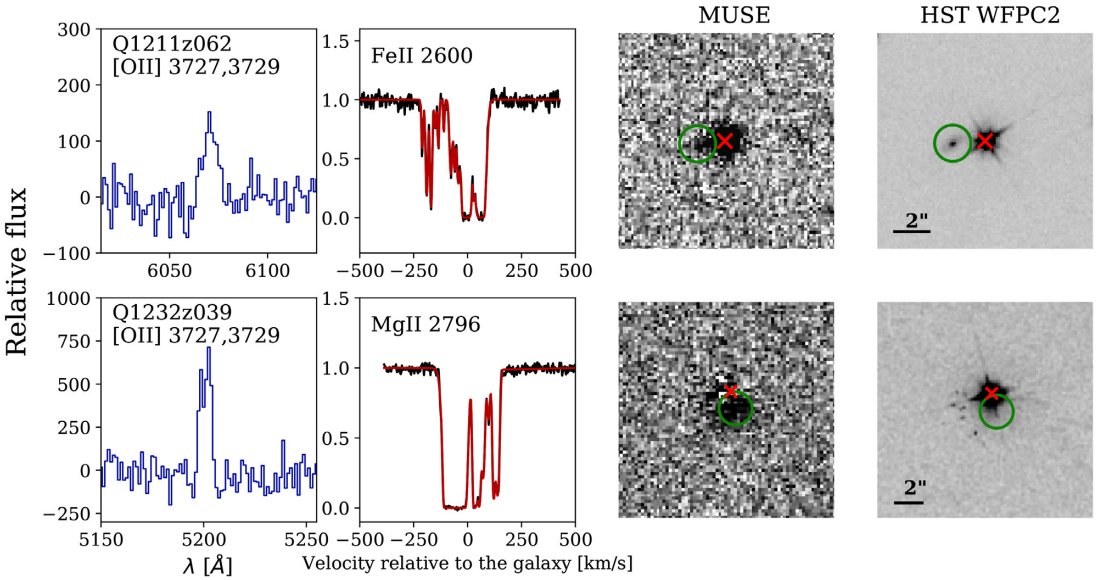

Figure 2. Spectral quasar PSF subtraction in the MUSE data. The panels present two galaxies, each hidden under the PSF of a different QSO, and their retrieved spectra: Q1211+1030 – top and Q1232-0224 – bottom. Galaxies were identified by detecting the [O II] emission line (first panel from the left) at the redshift of the absorber. To remove the quasar signature, we subtracted the continuum around the detected line. The second column presents the absorption lines detected in the normalized quasar spectrum in velocity space with zero velocity set to the systematic redshift of the galaxy. The third and fourth columns show the continuum-subtracted zoom-in MUSE image of the galaxy around the [O II] emission line and the zoom-in of the *HST* F702W image of the quasar on the same scale. The red cross represents the centre of the quasar and the green circle the position of the detected galaxy.

see more than one line (bright [O III] or H α). For the higher-z case ($z > 1.4$), the only observable emission line is Ly α (covered by MUSE at $z = 2.7$–6.7). Although theoretically, the detection could be a Ly α within that redshift range, based on the LAE luminosity function and the lack of the expected prominent asymmetric shape we exclude that interpretation.

We search for galaxies within $\Delta v \pm 1000$ km s^{-1} from the absorber. We measure the centre of the lines with a precision below 1 Å (corresponding to an error in the redshift estimation smaller than $\Delta z \pm 0.0003$). We note that the majority of galaxies lie within $\Delta v \pm 500$ km s^{-1}.

For three absorbers, Q1211z062, Q1232z039, and Q1130z031 (Péroux et al. 2019), we detect galaxies close to the quasar position (within 1 arcsec), blended with the quasar PSF. Spectral PSF subtraction allows for easier detection of such systems, despite the quasar bright contribution. In each case, we detected the [O II] emission doublet at the redshift of the absorber. We extracted the 1D spectrum of 4 × 4 spatial pixels around the line detection. The continuum of these objects is not detected. The method is illustrated in Fig. 2, for absorbers from two of the QSOs, where we present a zoom into the extracted spectrum around the [O II] emission line (in the observed wavelength frame), the main absorption feature of the associated absorber in the galaxy velocity space as well the pseudo-NB image alongside the *HST* image of the same region.

After NB identification of the sources at the redshift of the absorber, we extracted all continuum sources from the MUSE white light image using the MUSELET source finder, part of the MPDAF package provided by the MUSE GTO team (Bacon et al. 2016). MUSELET creates from a cube: (i) a white light image; (ii) R, G, B images corresponding to 1/3 of the wavelength range each; (iii) a set of NB images based on the average of five wavelength planes (total width of 6.25 Å). It then runs SEXTRACTOR (Bertin & Arnouts 1996) on these products, resulting in a catalogue of continuum sources. We classified all of the reported sources as either emission-line galaxies, absorption-line galaxies, stars, unknown continuum sources (without emission or absorption lines), or artefacts. We inspected all extracted spectra and used the [O II] and [O III] emission lines or the Ca K+H absorption lines to determine the redshift of each source. Among all galaxies associated with absorbers, we detected four passive galaxies (with only the Ca K+H absorption lines and red continuum). For completeness, we cross-matched the catalogue of continuum sources detected in MUSE with detections in archival *HST* WFPC2 images (Le Brun et al. 1997). This search led to no new galaxies discovered at the redshift of the absorbers. After the identification of the galaxies associated with the absorber on the white light continuum MUSE image, we measured their position with respect to the quasar. We fitted a 2D Gaussian to the continuum images of both the quasar and the galaxies to determine their geometrical centres and then measure the angular distance between them.

To test the completeness of the methods described above, we injected 100 mock sources into each MUSE data cube. The mock sources are single Gaussian emission lines of the integrated flux ranging from 10^{-21} to 10^{-17} erg s^{-1} cm^{-2}, represented spatially by a 2D Gaussian of FWHM of 3 pixels, corresponding to the MUSE PSF. We introduce the two types of mock sources: line emitters with continuum flux and without continuum. After running the MUSELET source extraction on these cubes, we compared the catalogue of detected sources with the list of mock sources. The completeness of our search is presented in Fig. 5. We are over 90 per cent complete for detections brighter than 23.5 mag for continuum objects and line flux greater than $10^{-17.7}$ erg cm^{-2} s^{-1}. We can retrieve sources down to the magnitude of 25.7 mag and flux $10^{-18.5}$ erg cm^{-2} s^{-1}.

We detected 43 associated galaxies within a 250 kpc impact parameter from the QSO sightline. As we summarize in Fig. 3, we detect systems with multiple galaxies associated with the absorber as well as a few systems where only one galaxy was detected.

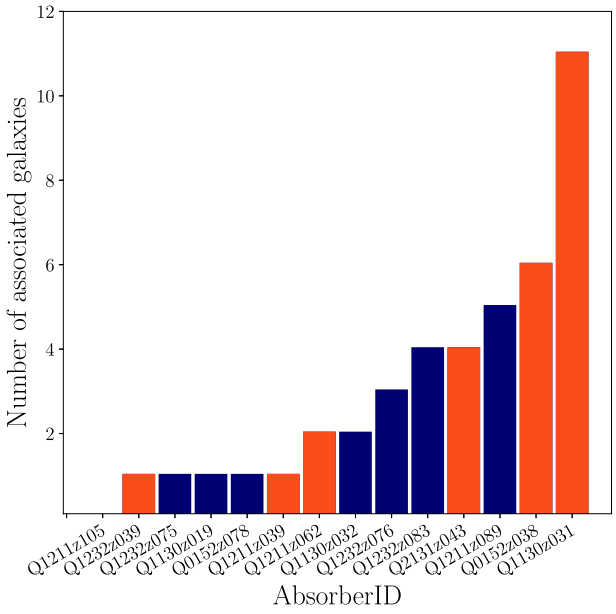

Figure 3. The number of galaxies associated with each absorber in our sample. H I-selected galaxies are indicated in orange, and metal-selected ones in blue. Most of the absorbers have two or more galaxies at the associated redshifts. Q1130z031 is an exceptionally rich galaxy group and also has the highest H I column density (Péroux et al. 2019). For Q1211z105, we do not detect any galaxy at the redshift of the absorber down to 0.1 $M_\odot$ yr^{-1}.

Only in one case we do not detect any associated galaxy. This results in a high detection rate of 93 per cent. Note that five of the absorbers in the sample were targeted MUSE observations of absorbers with a known counterpart. Nevertheless, among the remaining nine absorbers, we detect at least one galaxy for eight absorbers. Altogether, among the 14 absorbers, 8 (57 per cent) have more than one associated galaxy. This high detection rate is likely related to the combination of the wide field of view and simultaneous spectral coverage of MUSE. We are probing a large range of impact parameters, from low (<10 kpc) up to large distances of 200–250 kpc. We detect emission-line sources and passive galaxies with no emission lines but solely detected in continuum at the redshift of the absorbers down to an integrated line flux of $10^{-18.5}$ erg cm^{-2} s^{-1} and magnitude of 25.7 mag at the 20 per cent completeness level.

Table 2 summarizes the parameters of all absorbers and their associated galaxies. Spectra of all systems alongside their position marked on MUSE white light images and *HST* images are shown in Fig. 1 and in the appendix.

3.4 Measurements of the physical properties of galaxies associated with absorbers

The majority of the galaxies associated with absorbers in our sample are emission-line objects. We can use the measured line fluxes to calculate the SFRs of these galaxies as well as their emission-line metallicities. To obtain line fluxes, we fit Gaussian profiles to the [O II], [O III], H β, and H α emission lines (if detected), using the MPDAF Gaussian profile fitting tool. For the redshift estimation, we use [O II] $\lambda\lambda$3727, 3729 (fitted with double Gaussian profiles) as this line is detected in all galaxies. In the case of galaxies lacking emission lines, we used the Ca K+H absorption lines to determine the redshift.

For each galaxy, we compared the velocity offsets between the members of the group and the absorbing gas. In Fig. 4, we present the relative velocities of the galaxies of each absorbing system calculated with respect to the galaxy at the lowest impact parameter. Therefore, the velocity of the galaxy at the lowest impact parameter is set to zero. Additionally, we calculated the velocity between that galaxy and the absorbing gas. In four cases (out of eight multigalaxy systems), objects other than the closest galaxy are better aligned in velocity with the gas seen in the absorption.

For all emission-line galaxies in the sample (except Q1130z019, for which we used H α), the [O II] emission line is covered and detected. We used the flux of the line to calculate the SFRs of the galaxies following Kobulnicky et al. (1999). In Fig. 6, we present the measured SFR as a function of the redshifts of the absorbers. For sources for which we do not detect emission lines, we calculate the 3σ line limits at the expected line positions. We detect sources at the redshift of the absorbers down to an SFR of 0.01 $M_\odot$ yr^{-1} for $z < 0.4$ and 0.1 $M_\odot$ yr^{-1} for higher redshifts (Fig. 6). We report galaxies with a range of SFRs from passive galaxies (<0.1 $M_\odot$ yr^{-1}) to star-forming galaxies. Except for one case (23 $M_\odot$ yr^{-1}), the SFRs of associated galaxies range from 1 to 10 $M_\odot$ yr^{-1}. These values are not dust corrected since for objects most H α lies outside the probed wavelength range, thus making the measurement of Balmer Decrement, the reddening proxy, impossible. Note that the parameters taken from literature also do not have any dust correction applied.

To obtain the galaxy metallicities, we chose to use only those galaxies with measurements of the oxygen species [O II], [O III], and H β. We then used the R23 oxygen abundance calculation from Kobulnicky et al. (1999) as the metallicity proxy. This procedure results in two solutions: lower and upper metallicity branches. Ideally, additional parameters based on [N II] and H α can be used to differentiate between the branches. However, these lines are not covered with MUSE and therefore we present both the solutions. For passive galaxies, we use the line detection limits. For Q1211z089 and Q1232z083, the 12+log(O/H) values could not be determined because both [O III] and H β are outside of the MUSE wavelength coverage.

A comparison of the metallicity of the galaxies with that of the absorbing gas is shown in Fig. 7. Groups of galaxies associated with single absorbers are connected with vertical lines, and for most of the systems, the two metallicity branches are plotted. We mark the one-to-one relation with a black thick line in the lower part of the diagram. The red dashed line in Fig. 7 marks the emission-line metallicity limit of our measurements. For all measured systems, the galaxy metallicity is found to be higher than that of the absorbing gas although given the limits, the metallicities still could be consistent with the 1:1 relation. Note, however, that given the metallicity estimate caveats (see Section 3.1) these result must be taken with some caution. Finally, since we are not sensitive to metallicities below 12+log(O/H) = 7.5, we might be missing faint low-metallicity systems in our sample of galaxies associated with absorbers.

4 DISCUSSION

4.1 Absorbers are associated with multiple galaxies

The MUSE IFU proves to be an excellent instrument to search for galaxies associated with absorbers. The MUSE field of view of 1 arcmin translates to 200–250 kpc at redshift $z \sim 1$. Since each object comes with a spectrum, we can immediately classify all objects in

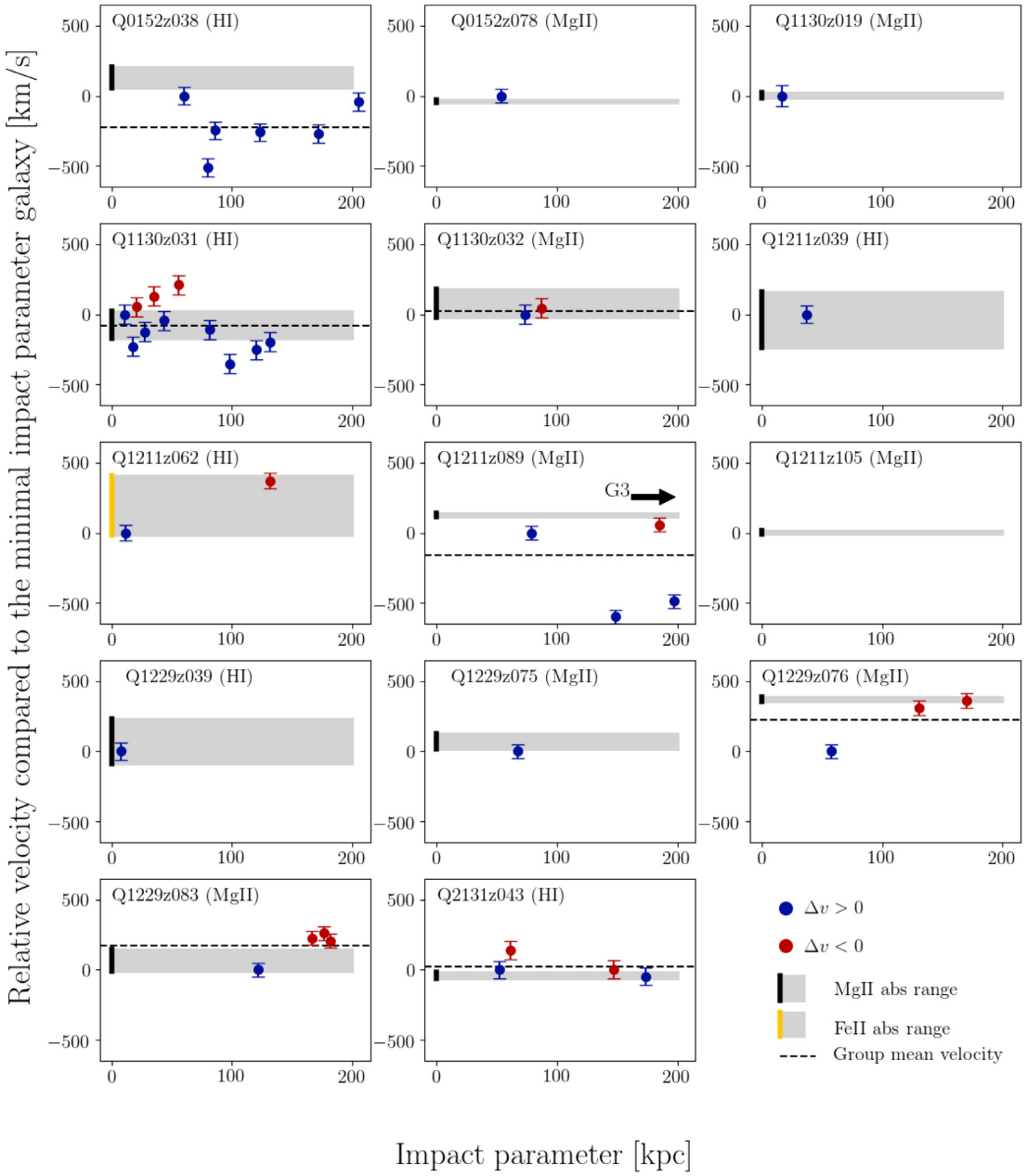

Figure 4. Impact parameter – velocity diagram of the MUSE-ALMA halo sample. The velocity of the galaxy at the lowest impact parameter is set to zero and the velocities of the remaining galaxies and absorption lines are calculated with respect to that galaxy. Galaxies with $\Delta v > 0$ are marked in red and with $\Delta v \leq 0$ in blue. The black line (and the further grey area) indicates the velocity span of all Mg II λ2796 absorption-line components. For the Q1211z062 system (marked in yellow), Mg II λ2796 was not covered and Fe II λ2600 was used instead. The dashed black line marks the mean velocity of the galaxy group. Note that galaxies with the smallest impact parameters are not always closest to the gas in velocity.

the field of view, including passive systems, increasing the extent of the search.

Furthermore, the identification of low-impact parameter galaxies (<1 arcsec) is also possible. Low-impact parameter sources are the primary candidates for the absorber hosts but can be potentially hidden under the extended PSF of bright quasars. Using spectral PSF subtraction, we can remove the quasar contamination and detect the emission lines from the source hidden under the PSF of the quasar (the method is described in Section 3.2). We report three such cases in our sample: Q1211z062, Q1232z039 (Fig. 2), and Q1130z031 (Péroux et al. 2019).

Candidates for galaxies associated with absorbers were traditionally identified on wide-field images and later confirmed using long-slit spectroscopy. A number of presumably unique galaxy–absorber pairs at different redshifts were discovered this way, supporting the picture of a CGM tracing the halo of a single galaxy. Wide-field IFU spectroscopy improved the completeness of the absorber counterpart search, resulting in discoveries of multiple galaxies

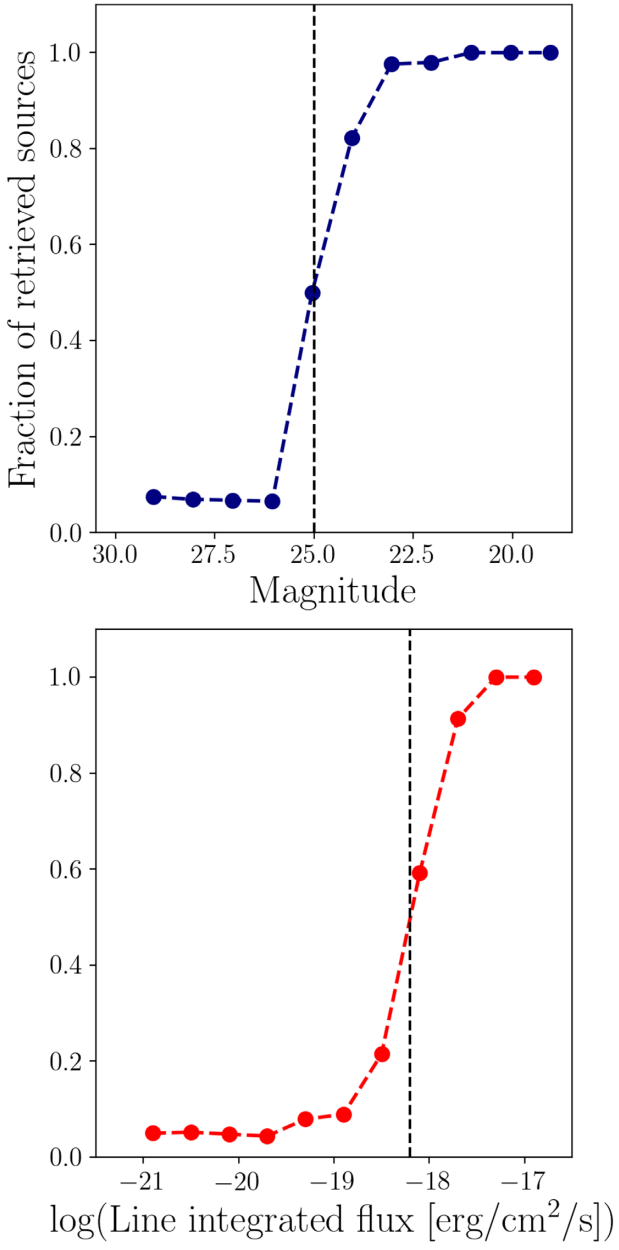

Figure 5. Completeness of the MUSELET search for continuum sources and line emitters in MUSE-ALMA halo MUSE cubes. Detection fractions of line emitters with continuum as a function of their magnitude are on the top panel (blue line) and of line emitters without detected continuum as a function of an integrated line flux are on the bottom panel (red line). The black dashed line marks the 50 per cent completeness level.

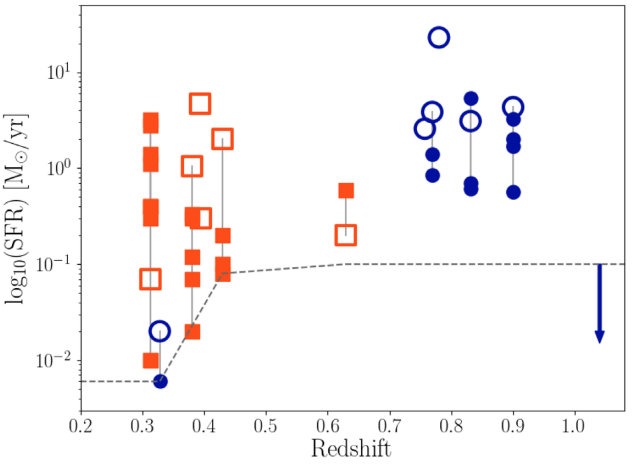

Figure 6. The star formation rate (SFR $_{[O\,II]}$) of the galaxies associated with absorbers as a function of redshift. The vertical grey lines connect galaxies associated with the same absorber. The open symbols indicate the galaxy at the smallest impact parameter. Absorbers selected based on their H I absorber are marked with orange squares, while metal-selected ones are marked with blue circles. The arrow marks the limits of the non-detection of the galaxy associated with the absorber Q1211z105. The dashed grey line represents the SFR limit at the redshift of the absorbers. We reach SFRs of 0.1 M$_\odot$ yr^{-1} for most of the sample and lower (about 0.01 M$_\odot$ yr^{-1}) in case of deeper data (Q1130−1449).

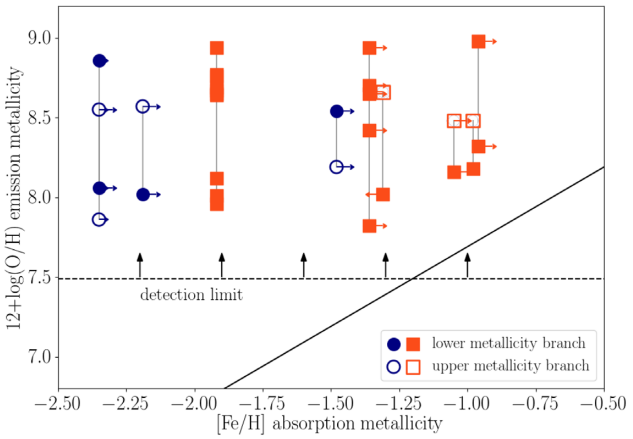

Figure 7. Oxygen abundance (emission metallicity) of the galaxies versus the metallicity of the absorbing gas. The solid black line represents the x=y line, and the grey dashed line marks the detection limit of our data. Galaxies associated with the same absorber are linked with a vertical line. The filled and hollow circles represent upper and lower metallicity branch solution. Absorbers selected based on their H I absorber are marked with orange squares, while metal-selected ones are marked with blue circles. Measurements from the literature with one solution are also plotted. In all cases where it is measured, the galaxy emission metallicity is larger than that of the absorbing gas.

associated with absorbers (Bielby et al. 2017; Klitsch et al. 2018; Bielby et al. 2019; Fossati et al. 2019). These findings also extend to higher redshifts with $z \sim 3$ DLAs associated with multiple LAEs, as in Mackenzie et al. (2019). Discoveries of multiple galaxies associated with low-z absorbers challenge the classical view of the CGM connected to the single halo of an isolated galaxy.

Cuts in both impact parameter and velocity difference between absorber and galaxy differ between published MUSE absorber studies, making the comparison of results not straightforward. MusE GAs FLOw and WInd (MEGAFLOW), a MUSE survey of Mg II absorbers, (Schroetter et al. 2016) allows for a 1000 km s^{-1} velocity difference between the galaxy and the absorber, and in case of multiple detections, the lowest impact parameter object is selected. Quasar Sightline And Galaxy Evolution (QSAGE), an O VI absorption oriented MUSE program (Bielby et al. 2019), supported by a larger impact parameter coverage with *HST* grisms, uses a tight limit of 400 km s^{-1} (expected outflow velocity). For sources covered only by *HST*, the velocity range is extended to 700 km s^{-1} to account for the lower resolution of the *HST* grism spectra compared

to MUSE. In a targeted single-system study, Bielby et al. (2017) find a galaxy group tightly aligned within $\Delta v = 140$ km s^{-1} around the absorber redshift, and within an impact parameter of 300 kpc, while in the case of a CO pre-selected absorber, Klitsch et al. (2018) looked for counterparts within $\pm$ 2000 km s^{-1}. In MUSE-ALMA haloes, we select galaxies to be associated with the absorber if their velocities do not differ by more than 1000 km s^{-1} from the absorber. Impact parameters are only limited by the MUSE field of view (up to 250 kpc at $z \sim 1$). We mostly detect systems with multiple galaxies associated with the absorber in velocity range between few km s^{-1} and $\pm$ 750 km s^{-1}. We used the luminosity function of [O II] emitters from Ly et al. (2007) to calculate the expected number of galaxies in the volume at the redshift of the absorbers. We find the expected number of detectable sources to be 0.45 for the higher redshift absorber and around 0.1 for the rest of the sample. Therefore, we conclude that we detect overdensities of galaxies associated with quasar absorbers, compared to random field galaxies.

Groups of galaxies typically include between 3 and 30 members and have a total dynamical mass of ($10^{12.5}$–10^{14}) h^{-1} M$_\odot$ with sizes between (0.1–1) h^{-1} Mpc (Bahcall 1996). Depending on mass, we would expect a velocity dispersion of group members between 100 and 500 km s^{-1} (Bahcall 1996). For the groups of absorption-selected galaxies in our sample, the velocity dispersion spans 160–350 km s^{-1}. Such values are typical of group environment.

Detecting multiple galaxies associated with the absorber introduces a complexity to the CGM–galaxy identification. Typically, absorbers at the lowest impact parameter would be considered the most likely counterpart for the absorber. Our analysis clearly demonstrates that impact parameters alone are not conclusive for identifying a unique galaxy associated with the quasar absorber. In Fig. 4 we present the velocity–impact parameter diagrams for all absorbers in our sample. In several cases, the galaxy at the lowest impact parameter is offset from the gas velocity by more than the typical galaxy rotation velocity (150–200 km s^{-1}). By contrast, some galaxies with larger impact parameter are better aligned to the absorbers velocity. This does not point directly to the gas origin since we also expect to see tracers of outflows in the CGM and wind velocities can be as high as 600 km s^{-1}. To link the absorbing gas with a particular galaxy, a detailed component-by-component analysis of the absorbing gas profile alongside resolved kinematic studies of the galaxy is needed.

To put our sample in the context of other known absorbers, we test if the galaxies follow the canonical relations. In Fig. 8, we present the H I column density versus impact parameter. Studies so far, mostly for high-H I column density absorbers (Krogager et al. 2017; Augustin et al. 2018), showed an anticorrelation between N(H I) and impact parameter, which is also reproduced by the OWLS hydrodynamical simulations (Rahmati & Schaye 2014): the larger the N(H I) column densities the smaller the impact parameter. Including all galaxies associated with absorbers, we are retrieving this relation also at lower H I column densities (from 10^{18} to $10^{21.7}$ cm^{-2}). Multiple associated galaxies, as in our sample, introduce a significant scatter into this relation.

All H I absorbers in our sample are also Mg II absorbers. Having both Ly α and Mg II for all systems is a unique quality of the sample. Typically, Mg II absorbers follow a W_r(2796) (Mg II λ2796 equivalent width) and impact parameter anticorrelation (e.g. Lanzetta & Bowen 1990; Bergeron & Boissé 1991; Bouché et al. 2006; Chen et al. 2010). We compared our groups to several other MUSE studies from the literature and the Mg II absorbers

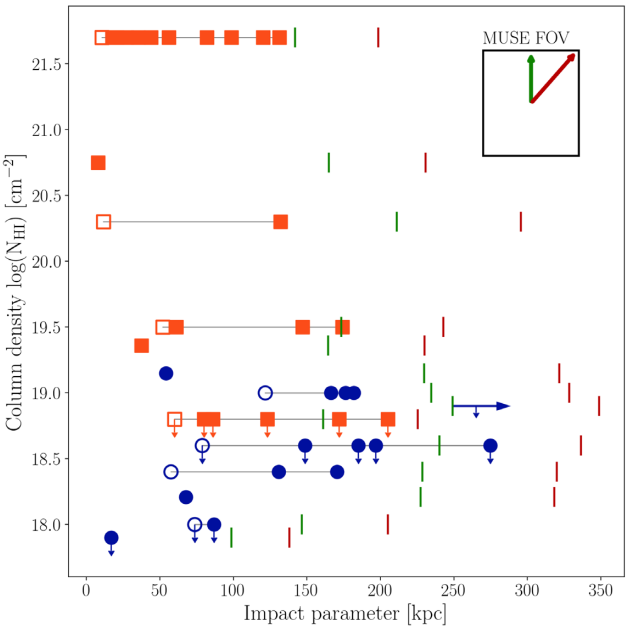

Figure 8. H I column density as a function of impact parameter. Absorbers selected based on their H I feature are marked with orange squares, while metal-selected ones are marked with blue circles. The blue, horizontal arrow marks the limits of the Q1211z105 associated galaxy impact parameter non-detection. The hollow symbols represent the lowest impact parameter object in groups. The red and green lines mark the limit of the impact parameter at the redshift of the absorber as defined by the MUSE field of view. Because the MUSE field of view is a square, we can reach larger impact parameters on the diagonal (red line) than along the square's side (green line; see the inset in the right upper corner). The horizontal grey lines connect galaxies associated with a single absorber. We find associated galaxies up to the impact parameters of 250 kpc.

compilation MAG IICAT (Nielsen et al. 2013) of isolated galaxies as well as galaxy groups (Nielsen et al. 2018). Fig. 9 shows that MUSE-ALMA halo systems are in agreement with this relation, especially with other absorption-related groups. Together with the group compilation from MAG IICAT, our data points seem to be offset from the 'individual' galaxies. Similar findings were reported by Bordoloi et al. (2011) in the COS-haloes comparison of Mg II absorbers in groups and isolated galaxies. The W_r(2796)–b relation for multiple associated galaxies define an envelope of possible parameters for the absorbers. Despite being sensitive to both low Mg II equivalent widths and low impact parameters, our observations do not populate the part of the plot with low W_r(2786) and low impact parameters.

Lowest impact parameter systems can lie far from the absorbing gas in velocity space, introducing the question of the nature of the gas detected in absorption and its physical connection with the galaxies detected in emission. A detailed component-by-component analysis of the metal absorption lines, together with resolved kinematic and metallicity maps of the galaxies, will likely provide information to identify the origin of the absorbing gas. Intra-group gas can be the result of the interactions between the group members, with possible higher density tidal streams or be filled with clouds of material infalling on to the centre of the group dark matter halo. This intra-group medium proves to be more complicated to describe and understand than a single halo picture, and is less straightforward to connect the inflow/outflow features with particular members of the group.

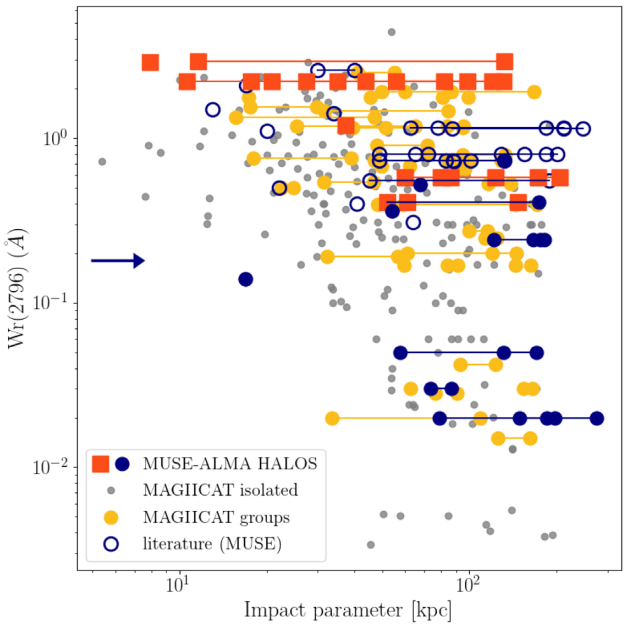

Figure 9. Mg II λ2796 absorption line equivalent width versus the impact parameter. The filled blue circles are the galaxies identified in MUSE-ALMA haloes (groups linked with a line, absorbers selected based on their H I feature are marked with orange squares); the open blue circles mark systems from the literature (Schroetter et al. 2016; Bielby et al. 2017; Klitsch et al. 2018; Zabl et al. 2019), groups are linked with lines. The blue, horizontal arrow marks the limits of the Q1211z105 with no detected associated galaxy. The underlying points come from the MAG IICAT catalogues of isolated galaxies and groups catalogues in grey and yellow, respectively. Groups of associated galaxies alongside isolated systems define a region in parameter space below which no absorbers are detected.

4.2 Metallicities of absorbers and associated galaxies

Measurements of H I and metal column densities of the absorbers in our sample give a unique opportunity to compare directly the metallicity of the gas and the integrated metallicity of the associated galaxies. Our absorption metallicity measurements suffer from several caveats, which can affect the results presented below (for the detailed discussion, see Section 3.1), and due to the lack of dust correction should be treated as lower limits. In Fig. 10, we present the difference of the metallicity of the gas and the galaxies as a function of the impact parameter. We find that in all cases the galaxy metallicity is higher than the gas metallicity lower limits. However, our detection threshold of emission metallicities goes down to 12+log(O/H) = 7.5, which corresponds to the absorbing gas metallicities.

Measuring the metallicity in two different spatial positions (in the associated galaxy and in the halo) can be interpreted as measuring a metallicity gradient. Resolved studies of nearby galaxies (like CALIFA or MaNGA) report negative ISM metallicity gradients in nearby star-forming galaxies (Sánchez et al. 2014; Ho 2016; Belfiore et al. 2017). Similar studies of high-redshift lensed galaxies have shown a diversity of gradients in star-forming galaxies (Queyrel et al. 2012; Jones et al. 2013, 2015; Leethochawalit et al. 2016). Positive metal gradients can point to strong outflows expelling metals to the CGM or suggest inflows of a large portion of metal-poor gas.

Expanding the metallicity gradients from the ISM to larger scales likely probes the physics of the CGM. Gradients between absorbing gas and galaxies were so far measured for systems with impact parameter below 100 kpc (Péroux et al. 2012; Christensen et al. 2014) and have an average value of −0.022 dex kpc^{-1}. Combining results from absorption spectroscopy of gravitationally lensed quasars with measurements for star-forming galaxies, isolated spirals, quasar–galaxy pairs, and gravitationally lensed galaxies, Kulkarni et al. (2019) also reported a tentative anticorrelation between the metallicity gradient and the metallicity at the galaxy centre: objects with low metallicity at the centre have positive metallicity gradients going outward.

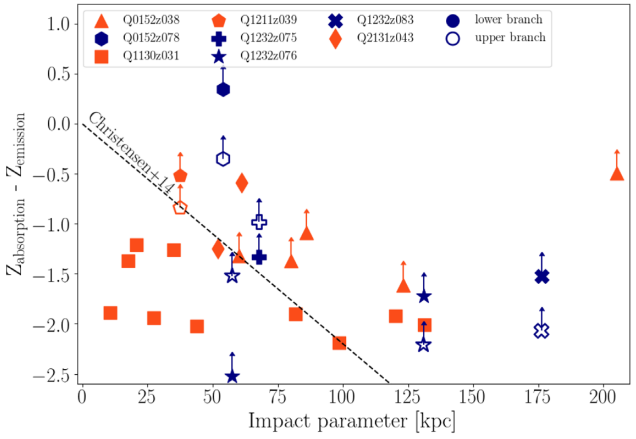

Figure 10. Difference in metallicity of the QSO absorption line and the metallicity from emission lines of the galaxies associated in redshift. Different symbols distinguish groups of galaxies associated with various absorbers; absorbers selected based on their H I feature are marked in orange. Filled symbols mark the lower branch metallicities or unequivocal values from the literature, and hollow symbols mark the upper metallicity branch. The dashed black line marks the CGM gradient measured by Christensen et al. (2014).

We looked at the difference between the absorber and galaxy metallicity as a function of impact parameter (Fig. 10). Note that our absorption metallicity measurements do not have detailed ionization correction, and additionally, we compare the values based on different elements: Fe for absorption and O for emission. We find no dependence of the metallicity difference on impact parameter and a larger scatter than Christensen et al. (2014) at redshift $0.1 < z < 3.2$. This is explained in part by the multiple galaxies associated with each absorber.

Hydrodynamical simulations like FIRE or IllustrisTNG (Muratov et al. 2015, 2017; Nelson et al. 2019) predict metals to be a tracer of the CGM structure following the flows of gas in and out of the galaxy. Metal-rich outflows are expected to originate in the centres of galaxies, introducing the metallicity differences with respect to the azimuthal angle between the quasar line of sight and the projected major axis of the galaxy. Future work will look these spacial variations of metallicity in more detail (see Péroux et al. 2016).

To relate the gas probed in absorption with the galaxies in the group, a detailed component-by-component analysis provides a promising avenue (Rahmani et al. 2018a; Rahmani et al., in preparation).

5 CONCLUSIONS

We report the first results of MUSE-ALMA haloes, a unique multiwavelength data set aimed at understanding the complexity of the CGM, the interactions with the galaxies, and the environmental effect on the high-H I column density absorbers. The survey consists

of 5 quasar fields for which we identified 14 absorbers at redshift $z < 1.4$. We searched for the galaxies associated with the absorber within the MUSE field of view (covering 200–250 kpc in impact parameter, depending of the system's redshift) and within $\Delta v = 1000$ km s^{-1} from the absorber redshift. Each absorber has an H I column density measured either from the literature or from archival FOS spectra. We used MUSE IFU observations to identify galaxies associated with the gas seen in absorption, finding altogether 43 such systems yielding a 89 per cent detection rate among the non-targeted absorbers. We find that most absorbers are associated with multiple galaxies or groups, tracing overdensities of at least a factor of 10 relative to the field galaxies. The detection of multiple galaxies is directly related to the ability to map a large field centred on the QSO, which is a unique capability of MUSE covering impact parameters up to 250 kpc. In addition, the use of spectral PSF subtraction for low impact parameter cases and the sensitivity of MUSE resulting in the detection of low-SFR object (SFR $>$ 0.01–0.1 M$_\odot$ yr^{-1}) allow for much more complete study of the galaxy environment linked to the absorber. The observed absorbing gas may then probe not only a single CGM halo but most likely the intra-group material affected by intergalactic interactions. By studying the relative velocity differences between the gas and the associated galaxies, we find that the traditional way of assigning the absorber to the lowest impact parameter galaxy should be challenged. We find large dispersion in velocities between galaxies and absorbing gas, sometimes pointing to a more distant galaxy as the main candidate for the host. We compare the parameters of the systems in our sample with canonical relations of the absorbers and their host galaxies, N(H I)–b and $W_r(2796)$–b. We find that the $W_r(2796)$–b relation follows the general trend while defining an envelope of parameters below which no further objects are detected. Thanks to our multiwavelength data set, we can compare the lower limits of metallicities of the absorbing gas with the metallicity of the galaxies as measured in the emission. We find that the overall metallicity is always higher in the associated galaxies than in the absorbing gas probed by the QSO. However, we are not sensitive to the low-metallicity systems below 12+(O/H) = 7.5, and gas metallicities are lower limits. Given the complexity of the environment associated with these absorbers, we advocate the use of the kinematics information that could assist in associating individual absorbing component with each galaxy member. A comparison to the resolved kinematic and ISM metallicity of the galaxies could improve our interpretation of the absorption lines. With this study, MUSE-ALMA haloes, we show that combining absorption and emission studies of CGM and associated galaxies is a powerful tool to study the evolution of gas inside and outside galaxies. In forthcoming work, we will study the molecular gas content of galaxies associated with the absorbers in our sample, using completed ALMA observations of all the quasar fields described in this work.

ACKNOWLEDGEMENTS

We thank the referee for the useful comments. CP thanks the Alexander von Humboldt Foundation for the granting of a Bessel Research Award held at MPA. AK acknowledges STFC grant ST/P000541/1 and Durham University. RA thanks CNRS and CNES (Centre National d'Etudes Spatiales) for support for her PhD. Authors thank C. Howk and N. Lehner for their comments and suggestions. AH thanks A. Bittner, M. Kozubal, and D. Wylezalek for comments that helped to improve this manuscript.

REFERENCES

Arrigoni Battaia F., Hennawi J. F., Prochaska J. X., Oñorbe J., Farina E. P., Cantalupo S., Lusso E., 2019, MNRAS, 482, 3162
Asplund M., Grevesse N., Sauval A. J., Scott P., 2009, ARA&A, 47, 481
Augustin R. et al., 2018, MNRAS, 478, 3120
Augustin R. et al., 2019, MNRAS, 489, 2417
Bacon R. et al., 2006, in McLean I. S., Iye M., eds, Proc. SPIE Conf. Ser. Vol. 6269, Ground-based and Airborne Instrumentation for Astronomy. SPIE, Bellingham, p. 62690J
Bacon R., Piqueras L., Conseil S., Richard J., Shepherd M., 2016, MPDAF: MUSE Python Data Analysis Framework, Astrophysics Source Code Library, record ascl:1611.003
Bahcall N. A., 1996, preprint (astro-ph/9612046)
Belfiore F. et al., 2017, MNRAS, 469, 151
Bergeron J., Boissé P., 1991, A&A, 243, 344
Bergeron J., Boulade O., Kunth D., Tytler D., Boksenberg A., Vigroux L., 1988, A&A, 191, 1
Bertin E., Arnouts S., 1996, A&AS, 117, 393
Bielby R., Crighton N. H. M., Fumagalli M., Morris S. L., Stott J. P., Tejos N., Cantalupo S., 2017, MNRAS, 468, 1373
Bielby R. M. et al., 2019, MNRAS, 486, 21
Boisse P., Le Brun V., Bergeron J., Deharveng J.-M., 1998, A&A, 333, 841
Bordoloi R. et al., 2011, ApJ, 743, 10
Borisova E. et al., 2016, ApJ, 831, 39
Bouché N., Murphy M. T., Péroux C., Csabai I., Wild V., 2006, MNRAS, 371, 495
Bouché N., Murphy M. T., Péroux C., Davies R., Eisenhauer F., Förster Schreiber N. M., Tacconi L., 2007, ApJ, 669, L5
Bouché N. et al., 2016, ApJ, 820, 121
Cantalupo S., Arrigoni-Battaia F., Prochaska J. X., Hennawi J. F., Madau P., 2014, Nature, 506, 63
Chen H.-W., Wild V., Tinker J. L., Gauthier J.-R., Helsby J. E., Shectman S. A., Thompson I. B., 2010, ApJ, 724, L176
Christensen L., Møller P., Fynbo J. P. U., Zafar T., 2014, MNRAS, 445, 225
Christensen L. et al., 2017, A&A, 608, A84
Corlies L., Peeples M. S., Tumlinson J., O'Shea B. W., Lehner N., Howk J. C., O'Meara J. M., 2018, preprint (arXiv:1811.05060)
Eisenhauer F. et al., 2003, in Iye M., Moorwood A. F. M., eds, Proc. SPIE Conf. Ser. Vol. 4841, Instrument Design and Performance for Optical/Infrared Ground-based Telescopes. SPIE, Bellingham, p. 1548
Ferland G. J. et al., 2013, RMxAA, 49, 137
Fossati M. et al., 2019, MNRAS, 490, 1451
Frank S. et al., 2012, MNRAS, 420, 1731
Fraternali F., 2017, in Fox A., Davé R., eds, Astrophysics and Space Science Library Vol. 430, Gas Accretion on to Galaxies. Springer, Cham, p. 323
Fumagalli M., O'Meara J. M., Prochaska J. X., 2016, MNRAS, 455, 4100
Fynbo J. P. U. et al., 2010, MNRAS, 408, 2128
Fynbo J. P. U. et al., 2013, MNRAS, 436, 361
Ho I. T., 2016, PhD thesis. Univ. Hawai'i at Manoa
Husemann B., Bennert V. N., Scharwächter J., Woo J. H., Choudhury O. S., 2016, MNRAS, 455, 1905
Jones T., Ellis R. S., Richard J., Jullo E., 2013, ApJ, 765, 48
Jones T. et al., 2015, AJ, 149, 107
Kacprzak G. G., Murphy M. T., Churchill C. W., 2010, MNRAS, 406, 445
Kacprzak G. G., Churchill C. W., Evans J. L., Murphy M. T., Steidel C. C., 2011, MNRAS, 416, 3118
Klitsch A., Péroux C., Zwaan M. A., Smail I., Oteo I., Biggs A. D., Popping G., Swinbank A. M., 2018, MNRAS, 475, 492
Kobulnicky H. A., Kennicutt Robert C. J., Pizagno J. L., 1999, ApJ, 514, 544
Krogager J. K., Møller P., Fynbo J. P. U., Noterdaeme P., 2017, MNRAS, 469, 2959
Kulkarni V. P., Cashman F. H., Lopez S., Ellison S. L., Som D., José Maureira M., 2019, ApJ, 886, 83
Lane W. M., Briggs F. H., Turnshek D. A., Rao S. M., 1998, Bulletin of the American Astronomical Society, 30, 1249
Lanzetta K. M., Bowen D., 1990, ApJ, 357, 321

Larkin J. et al., 2006, in Iye M., McLean I. S., eds, Proc. SPIE Conf. Ser. Vol. 6269, Ground-based and Airborne Instrumentation for Astronomy. SPIE, Bellingham, p. 62691A
Le Brun V., Bergeron J., Boisse P., Deharveng J. M., 1997, A&A, 321, 733
Leethochawalit N., Jones T. A., Ellis R. S., Stark D. P., Richard J., Zitrin A., Auger M., 2016, ApJ, 820, 84
Lehner N. et al., 2013, ApJ, 770, 138
Lofthouse E. K. et al., 2019, preprint (arXiv:1910.13458)
Lusso E. et al., 2019, MNRAS, 485, L62
Ly C. et al., 2007, ApJ, 657, 738
Mackenzie R. et al., 2019, MNRAS, 487, 5070
Martin C. L., Shapley A. E., Coil A. L., Kornei K. A., Bundy K., Weiner B. J., Noeske K. G., Schiminovich D., 2012, ApJ, 760, 127
Muratov A. L., Kereš D., Faucher-Giguère C.-A., Hopkins P. F., Quataert E., Murray N., 2015, MNRAS, 454, 2691
Muratov A. L. et al., 2017, MNRAS, 468, 4170
Muzahid S., Kacprzak G. G., Charlton J. C., Churchill C. W., 2016, ApJ, 823, 66
Muzahid S. et al., 2019, preprint (arXiv:1910.03593)
Møller P., Warren S. J., 1993, A&A, 270, 43
Møller P., Fynbo J. P. U., Fall S. M., 2004, A&A, 422, L33
Nelson D. et al., 2019, MNRAS, 490, 3234
Nielsen N. M., Churchill C. W., Kacprzak G. G., Murphy M. T., 2013, ApJ, 776, 114
Nielsen N. M., Kacprzak G. G., Pointon S. K., Churchill C. W., Murphy M. T., 2018, ApJ, 869, 153
Péroux C., Bouché N., Kulkarni V. P., York D. G., Vladilo G., 2011, MNRAS, 410, 2237
Péroux C., Bouché N., Kulkarni V. P., York D. G., Vladilo G., 2012, MNRAS, 419, 3060
Péroux C. et al., 2016, MNRAS, 457, 903
Péroux C. et al., 2017, MNRAS, 464, 2053
Péroux C. et al., 2019, MNRAS, 485, 1595
Prochaska J. X. et al., 2017, ApJ, 837, 169
Queyrel J. et al., 2012, A&A, 539, A93
Quiret S. et al., 2016, MNRAS, 458, 4074
Rahmani H. et al., 2016, MNRAS, 463, 980
Rahmani H. et al., 2018a, MNRAS, 474, 254
Rahmani H. et al., 2018b, MNRAS, 480, 5046
Rahmati A., Schaye J., 2014, MNRAS, 438, 529
Rao S. M., Turnshek D. A., Nestor D. B., 2006, ApJ, 636, 610
Rao S. M., Belfort-Mihalyi M., Turnshek D. A., Monier E. M., Nestor D. B., Quider A., 2011, MNRAS, 416, 1215
Rubin K. H. R., Prochaska J. X., Koo D. C., Phillips A. C., 2012, ApJ, 747, L26
Sánchez S. F. et al., 2014, A&A, 563, A49
Schroetter I. et al., 2016, ApJ, 833, 39
Schroetter I. et al., 2019, MNRAS, 490, 4368
Selsing J., Fynbo J. P. U., Christensen L., Krogager J.-K., 2016, A&A, 585, A87
Shull J. M., Danforth C. W., Tilton E. M., 2014, ApJ, 796, 49
Steidel C. C., Dickinson M., Persson S. E., 1994, ApJ, 437, L75
Tumlinson J., Peeples M. S., Werk J. K., 2017, ARA&A, 55, 389
Umehata H. et al., 2019, Science, 366, 97
Weilbacher P. M., Streicher O., Palsa R., 2016, MUSE-DRP: MUSE Data Reduction Pipeline, Astrophysics Source Code Library, record ascl:1610.004
Whiting M. T., Webster R. L., Francis P. J., 2006, MNRAS, 368, 341
Wisotzki L. et al., 2018, Nature, 562, 229
Wotta C. B., Lehner N., Howk J. C., O'Meara J. M., Oppenheimer B. D., Cooksey K. L., 2019, ApJ, 872, 81
Yanny B., Hamilton D., Schommer R. A., Williams T. B., York D. G., 1987, ApJ, 323, L19
Yanny B., York D. G., Gallagher J. S., 1989, ApJ, 338, 735
Yanny B., York D. G., Williams T. B., 1990a, ApJ, 351, 377
Yanny B., Barden S., Gallagher John S. I., York D. G., 1990b, ApJ, 352, 413
Zabl J. et al., 2019, MNRAS, 485, 1961
Zafar T., Popping A., Péroux C., 2013, A&A, 556, A140

APPENDIX A: DUST EXTINCTION

To test if dust depletion of metals in absorbers in our sample is significant, we fit a spectral template to the quasar spectra extracted from the MUSE cubes. We furthermore include optical (g, r, i, z, and y) and near-infrared photometry from PANSTARRS and 2MASS. We exclude photometric bands that are affected by strong emission lines (such as C IV and H α). Similarly, we exclude from the fit regions of the spectra that are affected by broad emission lines. The spectra are fitted using the quasar template spectrum by Selsing et al. (2016) including two free parameters: the rest-frame V-band reddening, A(V), and a variable intrinsic power-law index applied as an offset, $\Delta\beta$, relative to the template power-law index of $\beta_\lambda = -1.7$. This change in power-law index allows us to assess the impact of the unknown intrinsic quasar shape and propagate this uncertainty into the reddening estimate. We apply the reddening in the rest frame of the lowest redshift absorber (if more than one is present along the line of sight) as this will give the most conservative estimate of the reddening; less reddening is required for higher redshift absorbers. Lastly, the spectral template is normalized to match the observed flux level by including the nuisance parameter, f_0. In most cases, the best-fitting models are in good agreement with the data. We conclude that a low amount of dust reddening is the most probable solution.

APPENDIX B: GALAXY PROPERTIES

We present *HST* WFPC2 images with positions of galaxies associated with the absorbers described in this work (Figs A1–A6), as well as their spectra and continuum detection on MUSE white light images (A7–A14). MUSE white light and *HST* images for each quasar field present all detected galaxies associated with absorbers in our sample, differentiated by colours. Both images are in the same scale frame and oriented North up, East to the left. For clarity, we show the Q1130z031-rich group members on a separate figure (for details on this system, see Péroux et al. 2019).

Each spectrum panel gives the plot of the MUSE spectra of the galaxies from 4800 to 9300 Å except for the already published MUSE studies of Q0152z038 (Rahmani et al. 2018a), Q0152z078 (Rahmani et al. 2018b), Q1130z031 (Péroux et al. 2019), and Q2131z043 (Péroux et al. 2017). Emission lines in the galaxy are marked in red, as are the absorption lines of interstellar Ca II H&K from the galaxy. The spectrum of sky lines before subtraction is plotted in red. In the upper left-hand corner of each galaxy spectrum frame appears the identifier of the galaxy (first four digits of QSO right ascension, two decimal points of the absorber redshift (e.g. z019 for $z = 0.19$), and the galaxy ID (e.g. G1) with which the galaxy spectrum is associated, and the impact parameter (in kpc) of the QSO field images (Figs A1–A6) projected on to the plane perpendicular to the sightline of the QSO. Two postage stamps of the galaxy appear to the right of this label, above the spectra (from MUSE and from the WFPC on *HST*). If the *HST* inset is not present, the particular galaxy is outside the field of view of the *HST* WFPC2 camera. To the right of the galaxy spectrum is the spectrum of Mg II λ2796 or Fe II λ2600 for the absorption system noted in the galaxy spectrum frame (in rest-frame velocity units). The blue line is the normalized UVES/HIRES quasar spectrum, and red is a Voigt profile fit to the line. Because of the velocity span of some of the galaxies, not all panels are presented on the same velocity scale. We do not present among the spectrum figures the spectra of the galaxies extracted from the quasar PSF (Q1211z062-G1 and

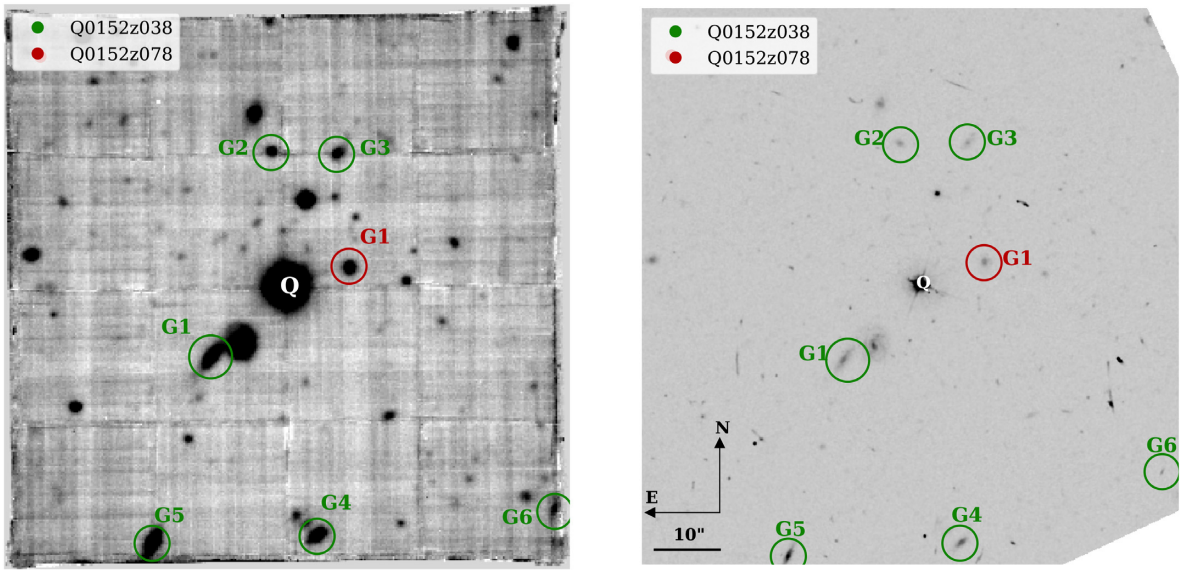

Figure B1. MUSE white light (left) and *HST* F702W (right) images of Q0152−2001 quasar field with galaxies associated with all absorbers marked. The green circles mark galaxies associated with Q0152z038 absorber, and red – Q0152z078 absorber. 'Q' indicates the quasar.

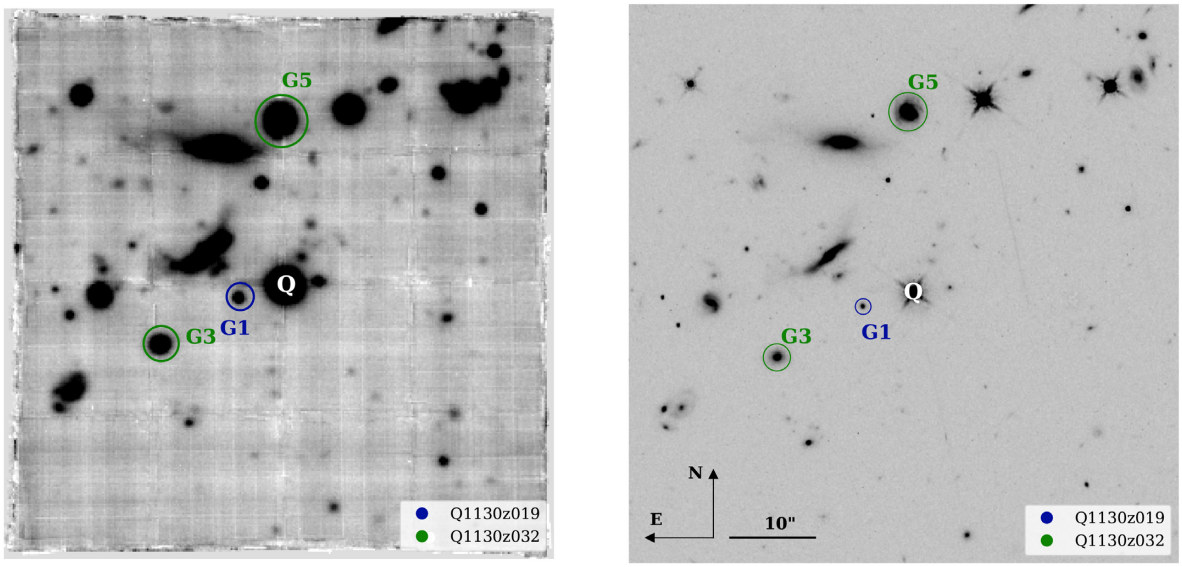

Figure B2. MUSE white light (left) and *HST* F104W IR (right) images of Q1130−1449 quasar field with galaxies associated with two absorbers marked. The blue circle marks the galaxy associated with Q1130z019 absorber, and green circle with Q1130z032 absorber. 'Q' indicates the quasar. The third absorber in this QSO, Q1130z031, is shown in Fig. B3.

Q1232z039-G1), because we were only able to retrieve the [O II] emission line with false continuum; they are presented in Fig. 2.

In the QSO fields (Figs A1–A6), each galaxy associated with an absorber is marked with a circle, colour coded by the absorber ID. The name of each absorber and a matching coloured dot matching appears in the upper left-hand or lower right-hand corner of the images of the QSO fields.

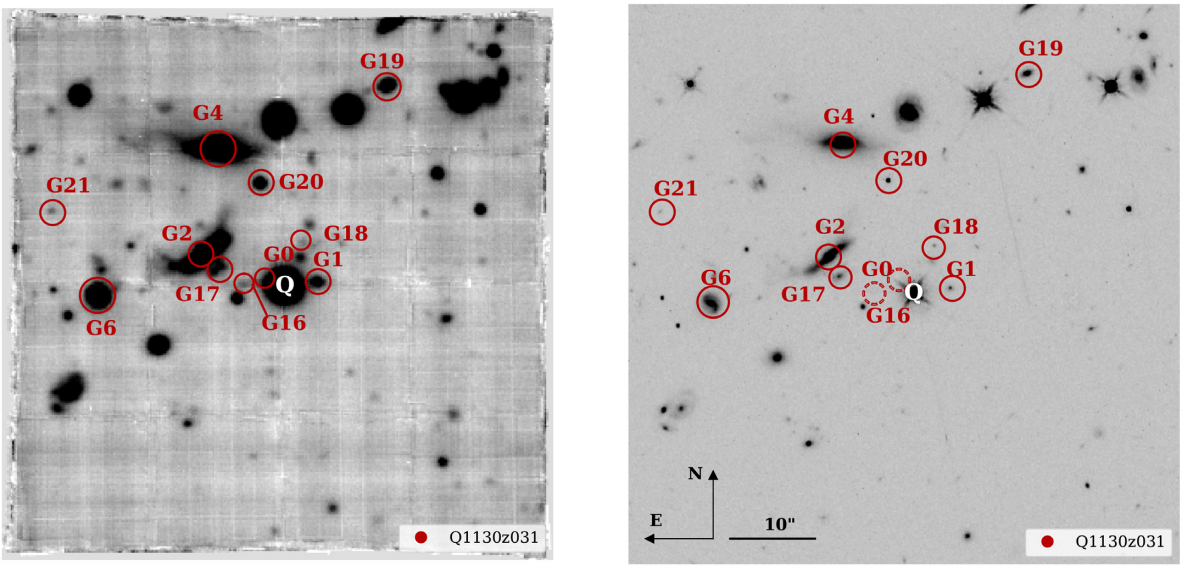

Figure B3. MUSE white light (left) and *HST* F104W IR (right) images of Q1130−1449 quasar field with galaxies associated with Q1130z031. Positions of galaxies not detected on the *HST* image (G0, G16) are marked with dashed circles. 'Q' indicates the quasar.

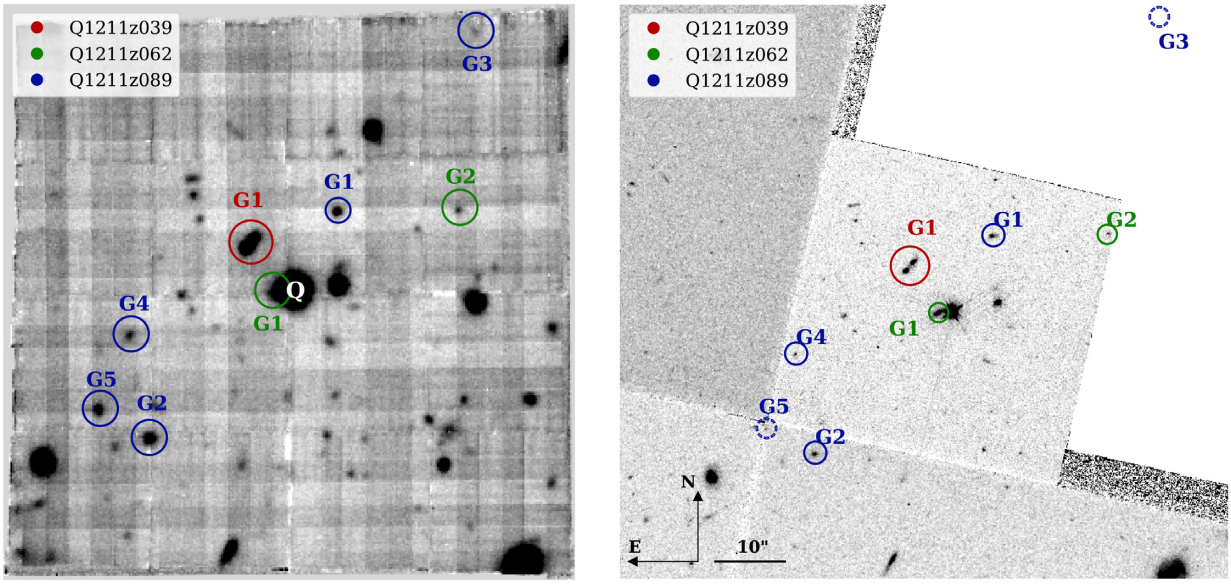

Figure B4. MUSE white light (left) and *HST* F702W (right) images of Q1211+1030 quasar field with galaxies associated with all absorbers marked. The red circles mark galaxies associated with Q1211z039 absorber, green – Q1211z062 absorber, and blue – Q1211z089 absorber. 'Q' indicates the quasar.

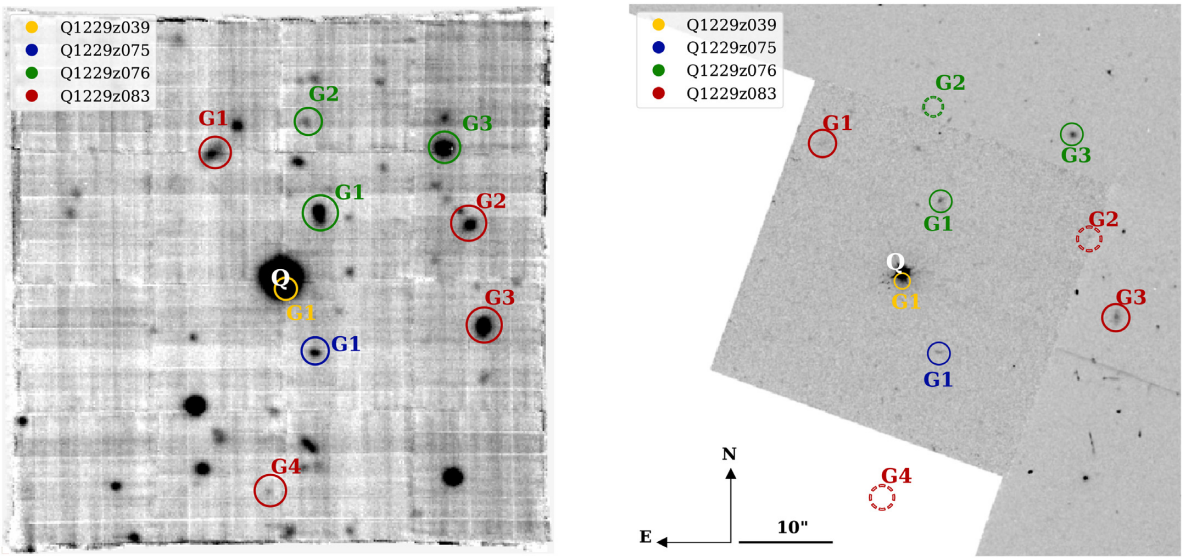

Figure B5. MUSE white light (left) and *HST* F702W (right) images of Q1232−0224 quasar field with galaxies associated with all absorbers marked. The yellow circles mark galaxies associated with Q1232z039 absorber, blue – Q1232z075 absorber, green – Q1229z076 absorber, and red with Q1232z083 absorber. 'Q' indicates the quasar.

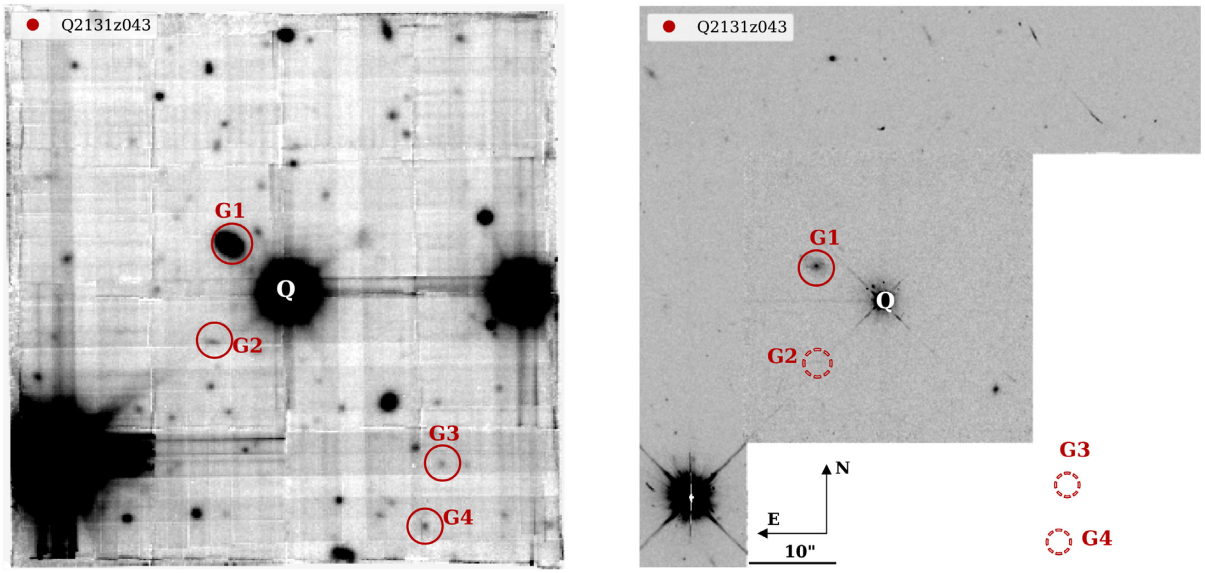

Figure B6. MUSE white light (left) and *HST* F702W (right) images of Q2131−1207 quasar field with galaxies associated with an absorber marked in red. The dashed circles mark the non-detections. 'Q' indicates the quasar.

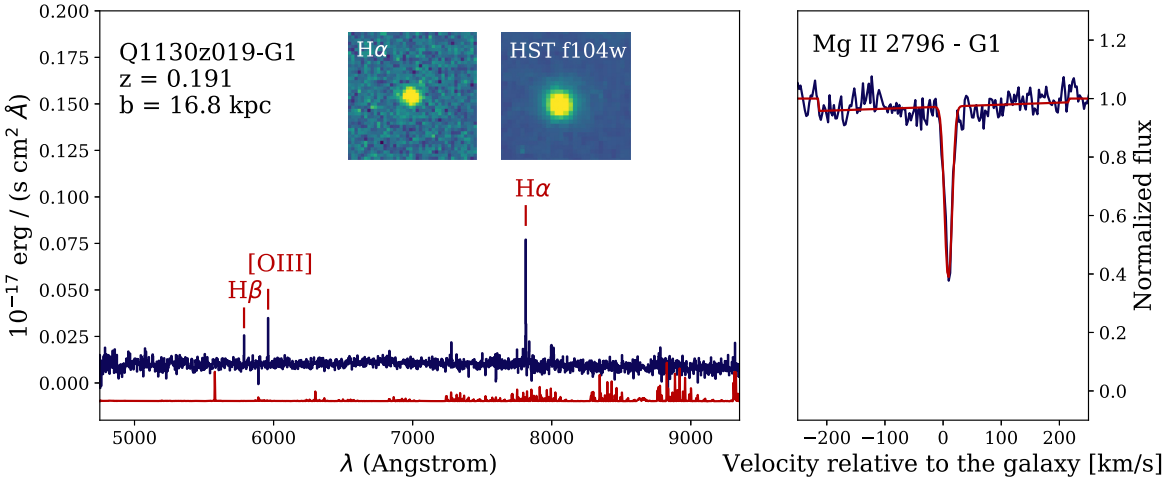

Figure B7. Q1130z019 absorber and associated galaxy (continuum images B2).

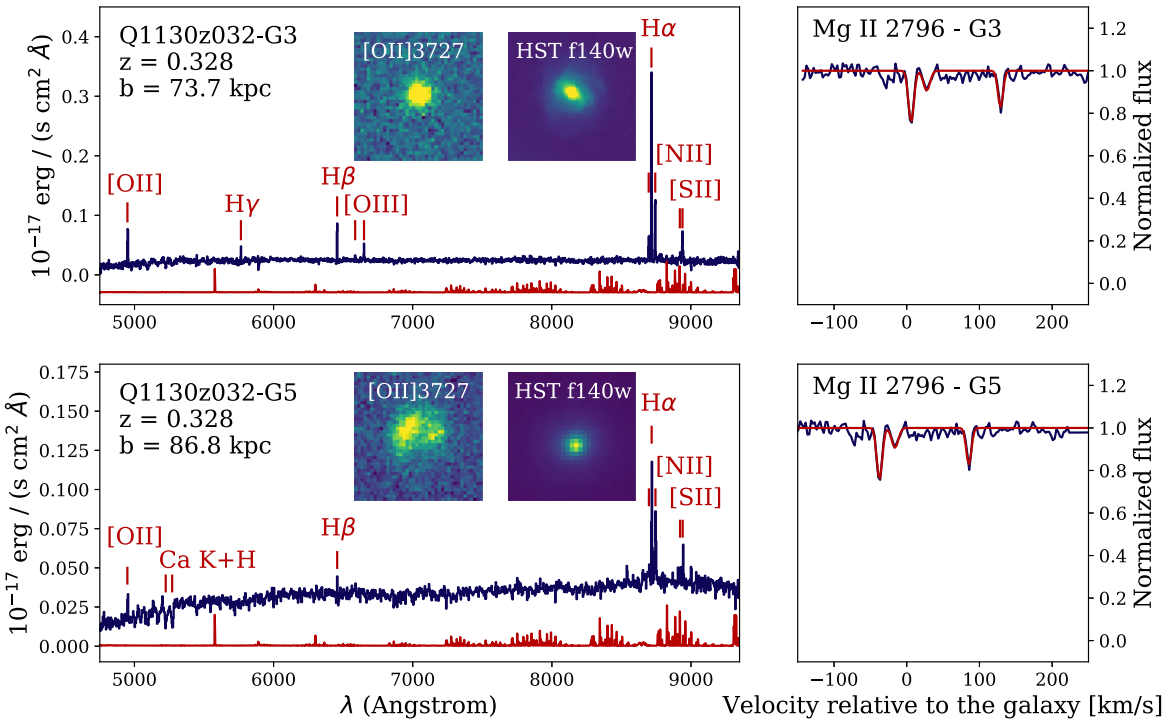

Figure B8. Q1130z032 absorber and associated galaxies (continuum images B2).

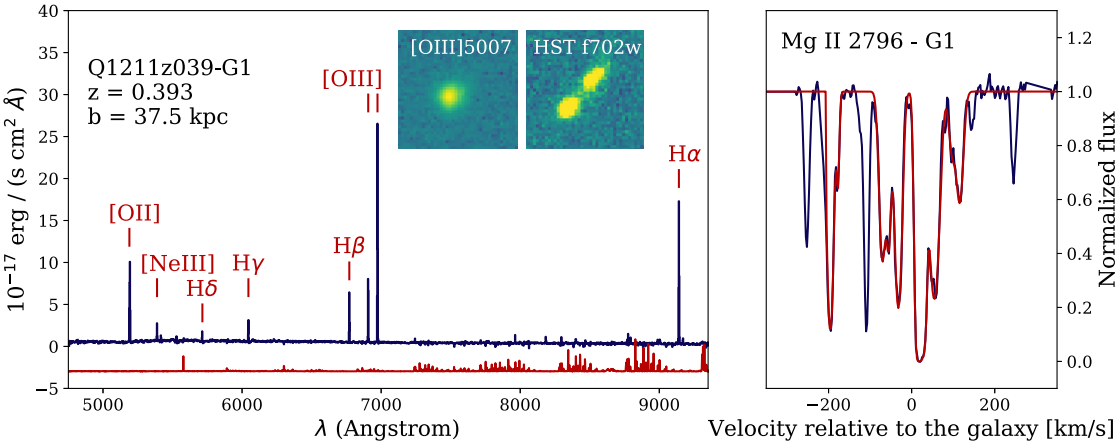

Figure B9. Q1211z039 absorber and associated galaxy (continuum images B4).

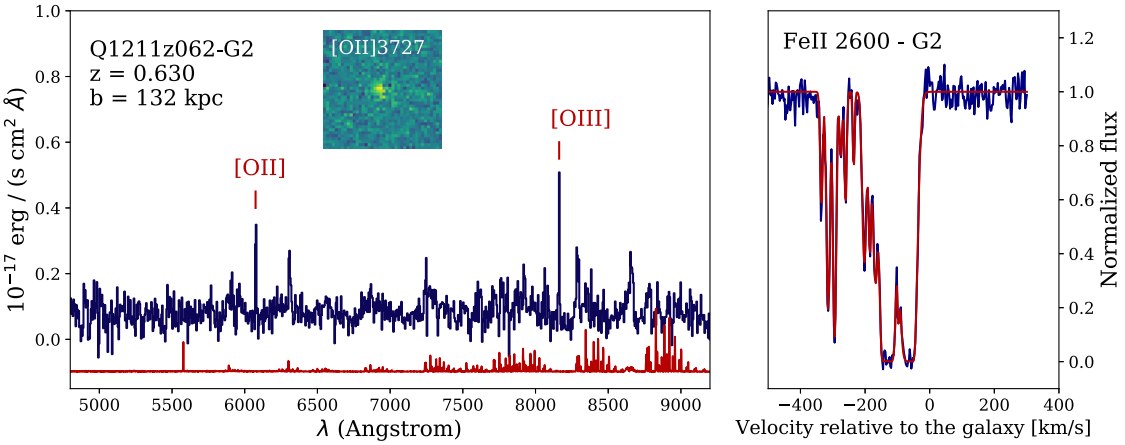

Figure B10. Q1211z062 absorber; G1 is a low-impact parameter associated galaxy, and only the [O II] emission line was extracted from the quasar PSF (presented in Fig. 2). Here we present only the spectrum of the second associated galaxy (G2). For this absorber, Mg II λ2796 falls in the UVES spectral gap, so we plot Fe II λ2600 profile instead (continuum images B4).

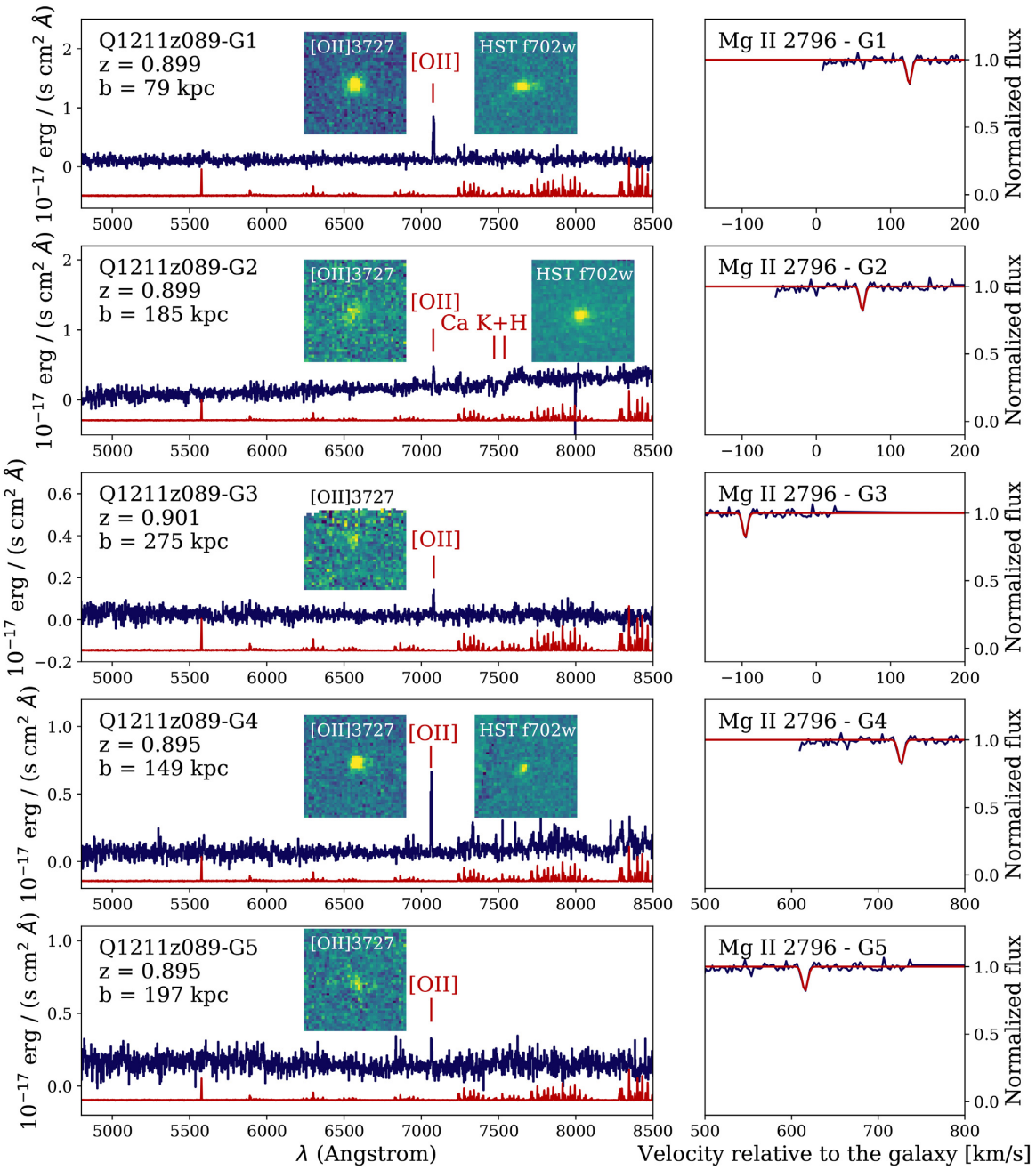

Figure B11. Q1211z089 absorber and associated galaxies. G3 is outside *HST* WFPC2 field of view, and G5 lies on the edge of the WF and PC chips of the *HST* WFPC2 camera and is not detected in continuum (continuum images B4). Note that due to larger velocity offset, G4 and G5 are presented in a different velocity range than G1–G3.

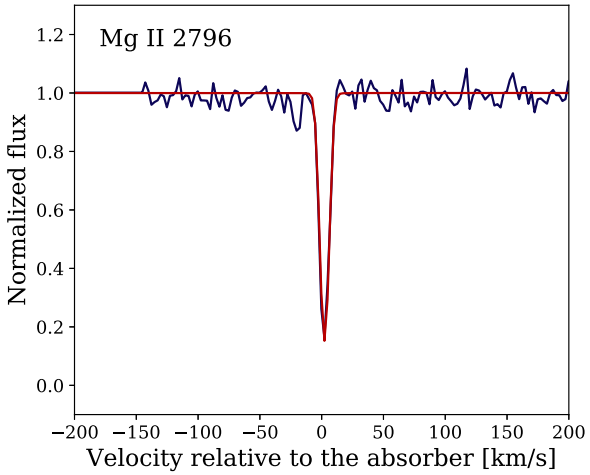

Figure B12. Q1211z105 absorber Mg II profile. This is the only absorber in the sample for which no associated galaxy was found.

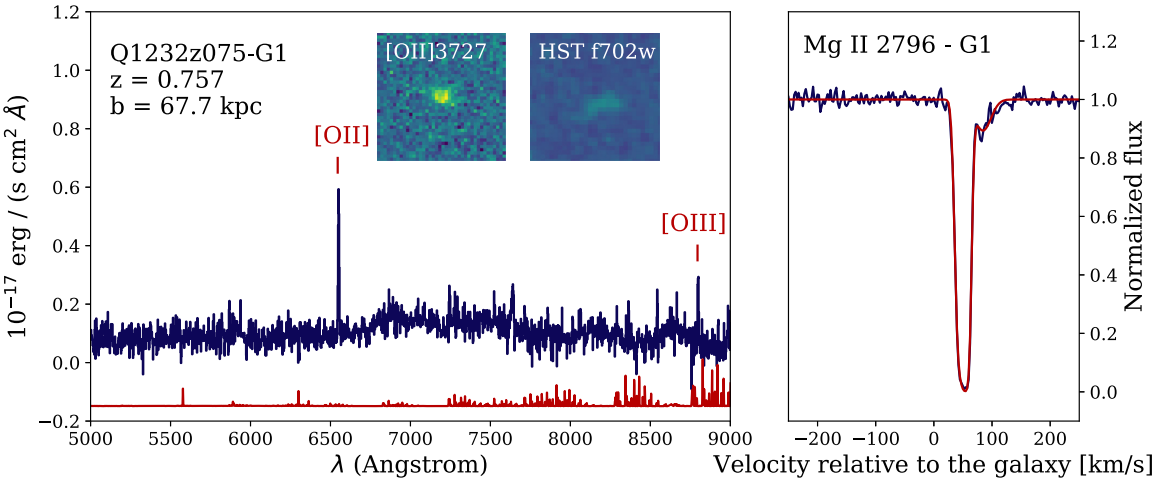

Figure B13. Q1232z075 absorber and associated galaxy (continuum images B5).

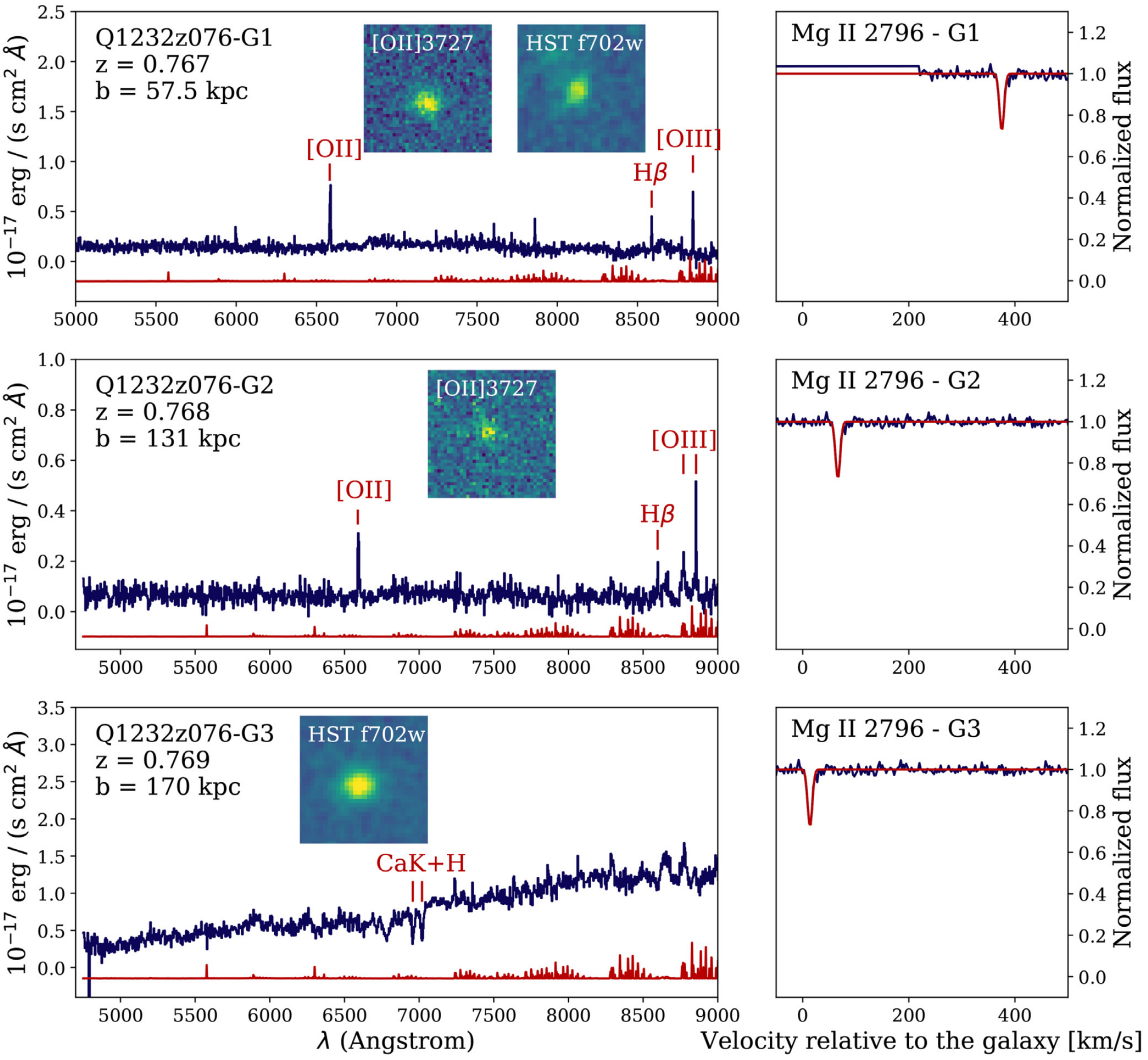

Figure B14. Q1232z076 absorber and associated galaxies. G3 is a quiescent galaxy with only absorption line and was detected only in continuum in MUSE white light image (continuum images B5).

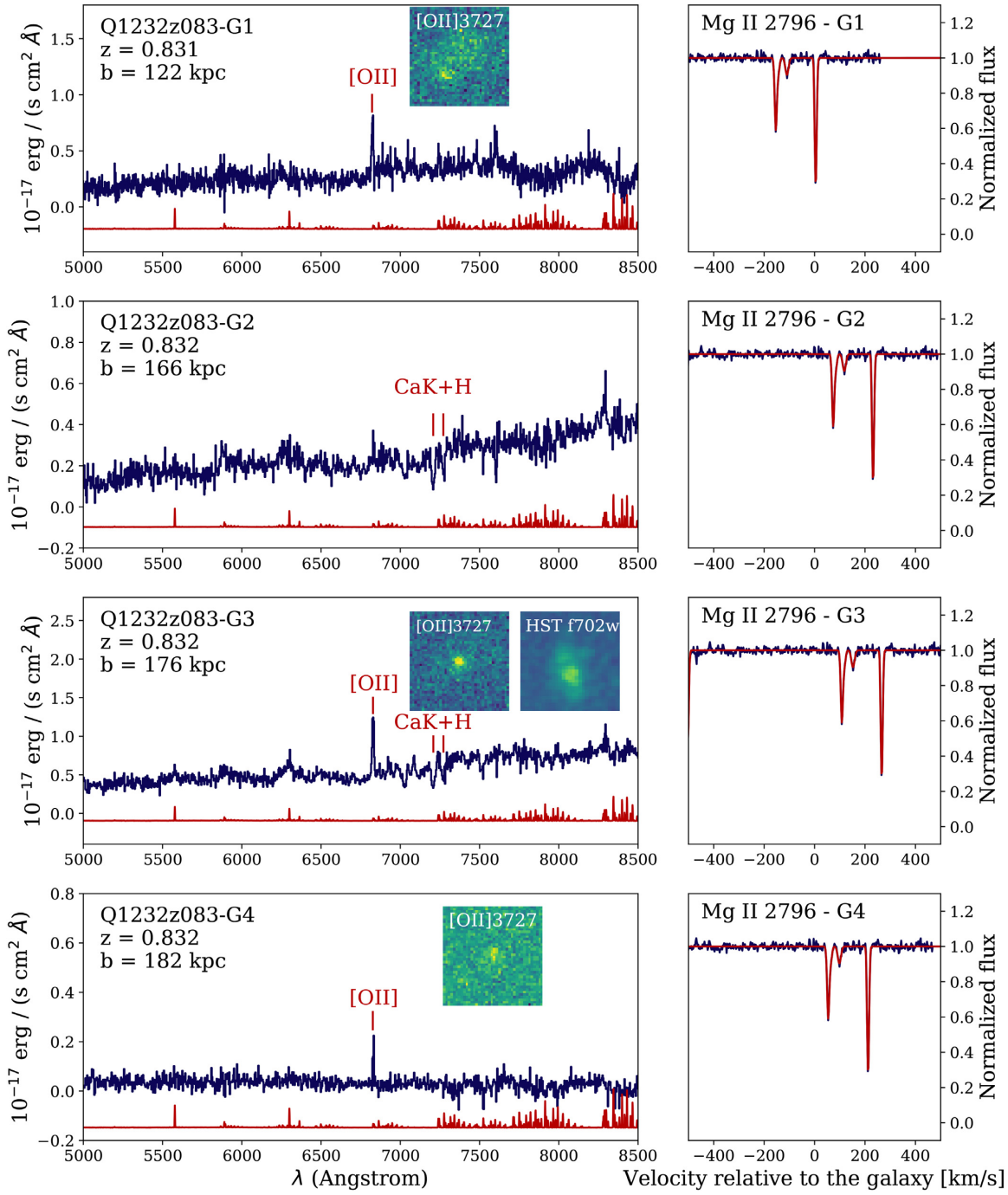

Figure B15. Q1232z083 absorber and associated galaxies G1 and G2 were not detected in continuum in *HST* image. G1 is very diffuse object; G2 is an absorption-line system, not detected in continuum in *HST* image; the inset presents only MUSE white light image centred at the galaxy (continuum images B5).

This paper has been typeset from a TEX/LATEX file prepared by the author.